Seismic performance of ultra-high performance concrete-filled FRP tube composite columns reinforced with SFCBs: Test and modeling

Item Type	Article
Authors	Zhang, Z.;Ashour, Ashraf;Ge, W.
Citation	Zhang Z, Ashour A and Ge W (2024) Seismic performance of ultra-high performance concrete-filled FRP tube composite columns reinforced with SFCBs: Test and modeling. Thin-Walled Structures. 205 (Part A): 112430.
DOI	https://doi.org/10.1016/j.tws.2024.112430
Rights	© 2024 Elsevier. Reproduced in accordance with the publisher's self-archiving policy. This manuscript version is made available under the CC-BY-NC-ND 4.0 license.
Download date	2026-02-16 12:32:54
Link to Item	http://hdl.handle.net/10454/20027

Seismic performance of ultra-high performance concrete-filled FRP tube composite columns reinforced with SFCBs: Test and modeling

Zhiwen Zhang[1], Ashraf Ashour[2], Wenjie Ge[1]*

1. College of Civil Science and Engineering, Yangzhou University, Yangzhou 225127, China;

2. Faculty of Engineering and Digital Technologies, University of Bradford, Bradford BD71DP, UK.

Abstract: To reduce residual deformation and address corrosion issues, this paper introduces a novel type of composite columns, utilizing ultra-high-performance concrete (UHPC)-filled fiber reinforced polymer (FRP) tubes (UHPC-FFT) and reinforced with steel-FRP composite bars (SFCBs). The seismic performance of the proposed SFCB-reinforced UHPC-FFT composite columns was evaluated through pseudo-static experiments and numerical analysis in comparison with those of traditional composite columns. Results indicated that the UHPC-FFT composite columns reinforced with SFCB exhibited larger energy dissipation compared with those reinforced with either steel or FRP bars. Increasing the axial compression ratio from 0.15 to 0.25 enhance load-bearing capacity but reduces ductility and energy dissipation. Increasing the yield strength of internal steel bar of SFCBs can improve the load-bearing capacity and deformation of the columns without affecting the ductility, initial stiffness, and stiffness degradation rate. Increasing the elastic modulus of out-wrapped FRP of SFCBs enhanced the seismic performance of UHPC-FFT composite columns but could lead to premature failure due to FRP rupture. It is recommended to set an elastic modulus for the outer FRP wrap at 55 GPa for optimal seismic performance in UHPC-FFT composite columns.

Keywords: UHPC-FFT composite column; SFCBs; seismic performance; pseudo-static test; numerical analyze

1 Introduction

Reinforced concrete (RC) structures in marine environments are exposed to long-term exposure to conditions such as salt spray and humidity, resulting in frequent steel rebar corrosion and concrete deterioration. These issues significantly compromise the durability and safety of structures [1]. Fiber reinforced polymer (FRP), as a lightweight, high-strength, and corrosion-resistant new material, holds promising potential for application in marine environments [2-4].

Concrete-filled FRP tube (CFFT) composite columns offer high ductility, exceptional corrosion resistance, improved strength and stiffness, reduced maintenance costs, lightweight construction, and enhanced seismic performance. Consequently, their performance has been the focus of numerous recent investigations [5-6]. The FRP tube provides effective confinement to the internal concrete, thus enhancing the overall structural performance [7-9]. Youm et al. [10] introduced an assembly-type CFFT column for rapid construction, that exhibited better seismic performance than that of RC columns, and was comparable to conventionally cast CFFT columns. Youssf et al. [11] concluded that stronger FRP confinement led to significant increases in both top displacement and bottom plastic hinge length of FRP-confined RC columns under horizontal loading. Li et al. [12] conducted quasi-static tests on basalt fiber reinforced polymer (BFRP) tube RC columns. The findings suggested that increasing the thickness of BFRP tubes had a limited effect on the load-carrying capacity and energy dissipation of the composite columns, while increasing the slenderness ratio resulted in slenderer hysteresis loops and significantly reduced load-carrying capacity, energy dissipation, and ductility. Fang et al. [13] investigated recycled aggregate concrete-filled FRP tube (RACFFT) composite columns through quasi-static tests. The results showed that the energy dissipation and ductility of recycled aggregate concrete-filled steel tube (RACFST) composite columns were higher than those of RACFFT composite columns but lower than those of recycled aggregate concrete-filled steel-FRP composite tube composite columns. Ren et al. [14-16] conducted quasi-static tests on FRP confined steel-reinforced recycled aggregate concrete columns (FCSRAC). Their test results concluded that, although the use of recycled aggregate concrete has a certain adverse effect on the load-capacity and stiffness degradation behavior of FCSRACs, their deformation capacity, energy dissipation capacity, and ductility can be improved with the use of recycled aggregate concrete. To mitigate stress concentration at corner angles in rectangular FRP-confined concrete, Zhang et al. [17-18] redesigned the section into an elliptical shape and placed longitudinal bars and H-shaped steel with welded shear studs inside the FRP tube to study the seismic performance of elliptical CFFT composite columns with different internal configurations. The results indicated that the aspect ratio had limited influence on the performance of elliptical CFFT composite columns; columns embedded with H-shaped steel exhibited greater energy dissipation and load-carrying capacity than those with longitudinal bars alone; and beyond a certain threshold, increasing the thickness of the FRP tube had limited effect on the seismic performance of the composite columns. In summary, in addition to common influencing factors such as axial compression ratio, FRP tube thickness, FRP type, infill concrete strength, and slenderness ratio, the form of longitudinal reinforcement within the tube also significantly affects the seismic performance of CFFT composite columns, particularly in regions with seismic risk.

Conventional RC structures often face challenges in controlling damage progression and minimizing residual deformations due to the minimal post-yield stiffness of rebars, leading to rapid damage development in the plastic phase [19-20]. Although reasonable design and verification can ensure the stability of structures during earthquakes, the formation of plastic hinges at the base can cause significant lateral displacement and excessive ductile deformation. To address these issues, recent research has employed FRP bars, utilizing their inherent benefits such as lightweight properties, superior strength [21-22], resistance to acid and alkali corrosion, and excellent recoverability. However, pure FRP materials exhibit linear elastic characteristics and lack a yield plateau similar to that of steel bars. Therefore, FRP-reinforced concrete structures exhibit poor ductility and are prone to brittle failure [23-24], making them less favorable, particularly in seismically active countries.

A novel steel-FRP composite bar (SFCB), featuring a steel core wrapped in FRP, has been recently developed to utilize the strength of each material. SFCB exhibits high strength, good ductility, high elastic modulus, stable secondary stiffness, and excellent corrosion resistance [25]. The mechanical properties of SFCB are essentially governed by these of both the internal steel reinforcement and the out-wrapped FRP. As a result, the elastic modulus of SFCB is lower than that of steel bar but higher than that of FRP bar with the same out-wrapped material. After yielding of internal steel bar, the elastic modulus of SFCB decreases as it mainly originates from out-wrapped FRP as the elastic modulus of internal steel bar tends to be zero, thus signifying the transition to post-yielding modulus. This post-yielding modulus represents the secondary stiffness. Benefiting from its higher post-yield stiffness, SFCB demonstrates superior tensile strength compared with steel bar while exhibiting lower tensile strength than FRP bar. Additionally, the cost of SFCB bars is positioned between that of steel and FRP bars, offering significant cost benefits relative to their characteristics. Sun et al. [26] conducted quasi-static tests and finite element analyses of SFCB-reinforced concrete columns, concluding that these columns exhibited continuously increasing load-carrying capacity after SFCB yielding, accompanied by minimal residual deformation and high post-earthquake reparability. In all, SFCB not only fundamentally addresses rebar corrosion issues but also achieves stable and controllable structural damage at the material level.

The current method utilized for fabricating SFCB involves the pultrusion process, which is a widely recognized and extensively employed industrial technique, as depicted in Fig. 1. Initially, steel bars are thoroughly cleaned and fiber bundles are thoroughly impregnated with resin. Secondly, through a mold with a specific cross-sectional shape, continuous extrusion and curing result in the production of high-quality SFCB. The critical interfaces of SFCB include the interface between steel bars and continuous fibers, as well as the outer surface of SFCB. The former ensures effective composite action between steel bars and fibers in SFCB, while the external surface ensures reliable bonding of SFCB with concrete, enabling its full effectiveness. Wu et al. [27] conducted uniaxial tensile tests on SFCBs with different surface treatments, demonstrating that using wrapped impregnated fibers effectively ensures good bonding performance at the composite interface between ribbed steel bars and out-wrapped fiber. Under high tensile strain, there was no slippage between FRP and internal steel bars, maintaining effective composite action between fibers and steel bars.

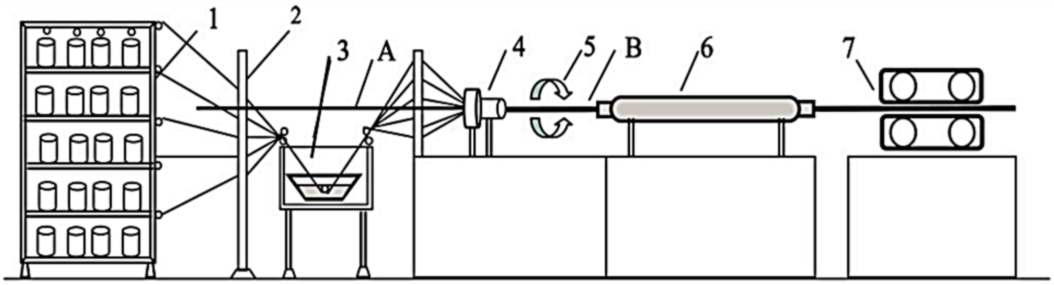

Fig. 1. Factory production of SFCB. Notes: 1- Roving frame; 2-Veil dispenser; 3-Immersion bath; 4-Preforming mould; 5-Electric winding plastic tape; 6-Constant temperature solidification furnace; 7-Traction equipment; A-Steel core; B-Out-wrapped FRP.

Ultra-high performance concrete (UHPC) exhibits superior mechanical properties, durability, and impermeability, effectively preventing corrosion from harsh environment [28-30]. Compare to normal strength concrete (NSC), UHPC significantly enhances the load-bearing capacity, ductility, and energy absorption capabilities of structures [31-32]. As UHPC preparation technology continues to advance, there is an urgent need for further research on the mechanical properties of UHPC in various structural forms. To date, there has been limited research conducted on the mechanical properties of UHPC structures reinforced with SFCBs. The flexural performance of UHPC beams reinforced with SFCB was investigated by Ge et al. [33-34] through four-point bending tests and finite element modeling (FEM). The results demonstrated that, compared with beams solely reinforced with FRP, those reinforced with SFCB exhibited a distinct yielding phase in the load-deflection curve. Moreover, substituting FRP with SFCB at the same reinforcement ratio shifted the failure mode of the beam from brittle to ductile. Combining SFCB, which offers high strength, durability, and stable secondary stiffness, with UHPC, known for its high strength, durability, and toughness, not only addresses issues related to structural corrosion and enhances structural durability but also imparts exceptional electromagnetic interference resistance to the structure. This makes the SFCB-reinforced UHPC structures ideally suited for applications in buildings requiring electromagnetic shielding, such as airports, radar stations, high-speed rail tracks, and bridges. By integrating FRP tubes, SFCB, and UHPC, the UHPC-filled FRP tube (UHPC-FFT) composite columns reinforced with SFCB can fully leverage the advantages of each component, achieving a powerful synergistic effect.

Based on the aforementioned concept, this study proposes a novel type of composite column that utilizes UHPC-FFT reinforced with SFCBs. This study investigates the behavior of SFCB-reinforced UHPC-FFT composite columns through quasi-static tests and FEM. The effect of reinforcement type, axial compression ratio, tube material type and concrete type on the seismic performance of these columns was evaluated. The FEM validated models explore the impacts of additional parameters, including the slenderness ratio, thickness of FRP tube, reinforcement ratio and sectional configurations of SFCB (sectional steel ratio of SFCB, yield strength of core steel, elastic modulus and ultimate tensile strength of out-wrapped FRP), providing corresponding structural design recommendations of these columns. This research serves as a theoretical reference for the structural design and widespread application of SFCB-reinforced UHPC-FFT composite columns.

2 Materials

2.1 Concrete

Table 1 presents the mass ratios of various ingredients used in NSC and UHPC. In accordance with the Chinese code JGJ/T 55-2019 [35], the fine aggregate for NSC consists of manufactured sand with an average particle size of 0.5 mm and ordinary Portland cement of grade P.II 42.5, while the coarse aggregate comprises crushed stone with particle sizes ranging from 5 mm to 20 mm. The raw materials of UHPC are displayed in Fig. 2, while Table 2 presents the fundamental ingredients (mass ratio) of UHPC, where *w*/*b* is the water-binder ratio, V_s is the volume fraction of steel fiber. According to the Chinese code GB/T 31387-2015 [36], UHPC incorporates manufactured sand with an average particle size of 0.5 mm, and Portland cement of grade P.II 52.5. Additionally, the active mineral admixtures include 400 mesh silica fume, slag powder grade S95, and fly ash grade II. Copper-plated steel fibers have a diameter of 0.22 mm, a length of 13 mm, no hooks at the ends, and a tensile strength greater than 2850 MPa were used. Local tap-water was used as mixing water. The polycarboxylate superplasticizer with a solid content of 30% and a water reduction rate of 40% was used.

(a) Cement (P.II 52.5) (b) Silica fume (c) Slag powder

(d) Fly ash (e) Manufactured sand (f) Steel fiber

Fig. 2. Raw materials of UHPC.

Table 1. Mixture proportions by weight of NSC and UHPC.

Concrete	*w*/*b*	Cement	Sand	Stone	Slag powder	Silica fume	Fly ash	V_s (%)	Superplasticizer (%)
NSC	0.42	1.0	1.64	2.67	/	/	/	/	1.05
UHPC	0.19	0.55	1.2	/	0.1	0.25	0.1	1.0	1.5

Table 2. Chemical properties of cement and mineral admixtures (unit: %).

Material	SiO_2	Al_2O_3	CaO	MgO	Fe_2O_3	Na_2O	TiO_2	SO_3	K_2O
Cement	19.06	4.71	66.17	—	3.49	—	—	2.40	0.46
Fly ash	54.76	24.56	4.85	0.10	6.54	—	1.85	—	—
Silica fume	96.74	0.32	0.11	0.10	0.08	0.09	—	—	—
Slag powder	32.80	15.36	37.12	8.52	0.74	—	1.95	—	—

Mechanical tests of NSC and UHPC were carried out according to Chinese codes GB/T 50081-2019 [37] and T/CBMF 37-2018, T/CCPA 7-2018 [38], respectively. Three cubic concrete specimens (100 × 100 × 100 mm) were prepared for compression test, along with three dumbbell-shaped concrete specimens for tensile test. These specimens were cured in the same environment as the main composite beams. The measured average cubic compressive strength for NSC and UHPC are 36.1 MPa and 102 MPa, respectively, while the average tensile strengths are 2.45 MPa and 7.51 MPa, respectively. Figure 3 illustrates the measured stress-strain curves for UHPC.

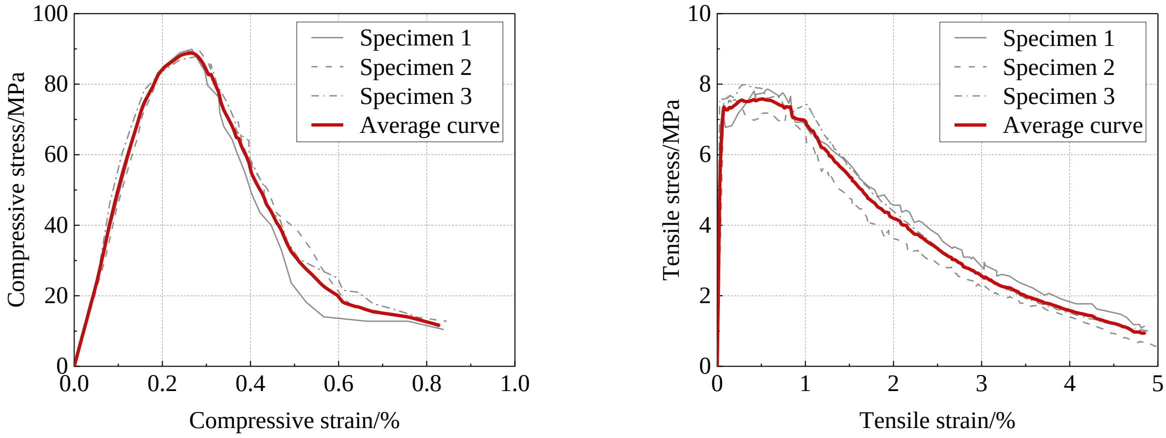

(a) Compression (b) Tension

Fig. 3. Stress-strain curves of UHPC.

2.2 Reinforcement

Figure 4 illustrates the photograph of reinforcements and the schematic diagram of SFCB. Three different types of reinforcing materials were employed, namely conventional steel bars, BFRP bars and SFCB. Both the conventional steel bar and the inner core of the SFCB consist of HRB400-grade steel, while the outer wrapping of the SFCB comprises BFRP. Table 3 outlines the detailed parameters of the reinforcements. Where, s_r and d_r are the spacing and depth of ribs, respectively; d_s and d are the inner steel diameter and overall diameter of each bar, respectively; t_f indicates the thickness of the out-wrapped FRP; a_s represents the sectional steel ratio, that is the ratio of the inner core steel area to the total sectional area of the SFCB.

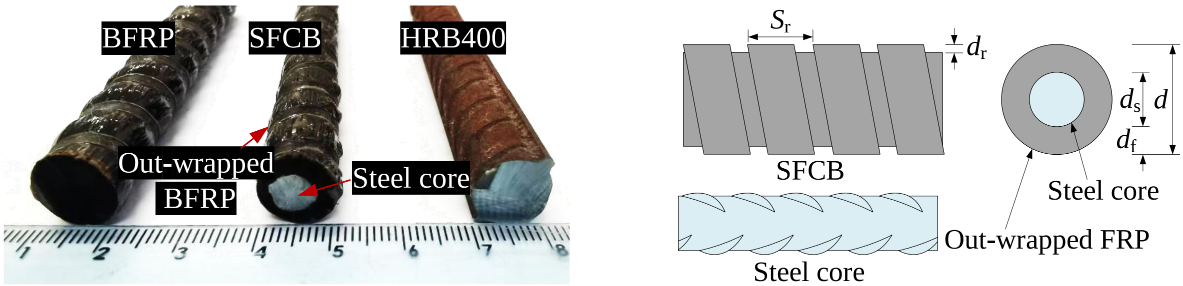

(a) Reinforcements (b) Schematic diagram of SFCB

Fig. 4. Reinforcements used and the schematic diagram of SFCB.

Table 3. Details of the reinforcements.

Reinforcement	d/mm	d_s/mm	t_f/mm	d_r/mm	s_r/mm	a_s
Steel bar	12	12	0	1.2	8.0	1.00
SFCB	12	6	3	1.5	10.0	0.25
BFRP bar	12	0	6	1.5	10.0	0

According to ASTM D7205/D7205M-21 [39], uniaxial tensile tests were conducted on the three types of reinforcements. For HRB400-graded steel bar, the yield strength and ultimate strength were measured at 485 MPa and 586 MPa respectively, with an elastic modulus of 200 GPa. The BFRP bar exhibited an ultimate strength of 1002 MPa and an elastic modulus of 44 GPa. SFCB showed a yield strength of 210 MPa and an ultimate strength of 808 MPa, with initial and post-yield elastic moduli measured at 82.5 GPa and 35.5 GPa respectively. Figure 5 illustrates the uniaxial tensile test setup along with the stress-strain (σ_s-ε_s) curves for all reinforcements. The uniaxial tensile stress-strain relationship for SFCB can be derived from the material composite law [40], as shown in Eq. (1). Where, $\varepsilon_{sf,y}$ and $\varepsilon_{sf,u}$ represent the yield strain and ultimate tensile strain for SFCB, respectively; $E_{sf,1}$ and $E_{sf,2}$ are the initial elastic modulus and post-yield elastic modulus for SFCB, respectively; $A_{sf,s}$ and $A_{sf,f}$ are the cross-sectional areas corresponding to the inner core steel and outer FRP wrap, respectively; and A_{sf} represents the total cross-sectional area of SFCB.

$$\sigma_s = \begin{cases} E_{sf,1}\varepsilon_s & 0 < \varepsilon_s \le \varepsilon_{sf,y} \\ E_{sf,1}\varepsilon_{sf,y} + E_{sf,2}\left(\varepsilon_s - \varepsilon_{sf,y}\right) & \varepsilon_{sf,y} < \varepsilon_s \le \varepsilon_{sf,u} \end{cases} \tag{1}$$

$$E_{sf,1} = \left(E_s A_{sf,s} + E_f A_{sf,f}\right) / A_{sf} \tag{2}$$

$$E_{sf,2} = E_f A_{sf,f} / A_{sf} \tag{3}$$

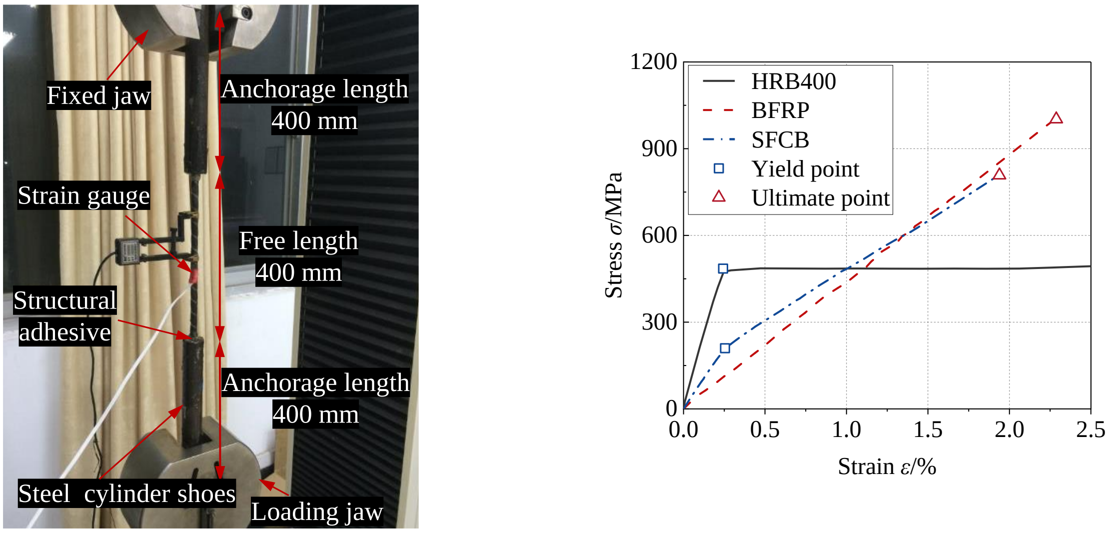

(a) Tensile test setup (b) Tensile stress-strain curves

Fig. 5. Uniaxial tensile test of steel bar, SFCB and BFRP bar.

2.3 FRP/steel tube

The mechanical test of FRP tube is presented in Fig. 6. In accordance with the Chinese code GB/T 5350-2005 [41], vertical compression tests were conducted on FRP tubes, resulting in a vertical compressive strength of 106 MPa and an elastic modulus of 7.22 GPa. Referring to ASTM D2290-19a [42], the hoop tensile strength of FRP tubes is 385 MPa, accompanied by an elastic modulus of 33.4 GPa.

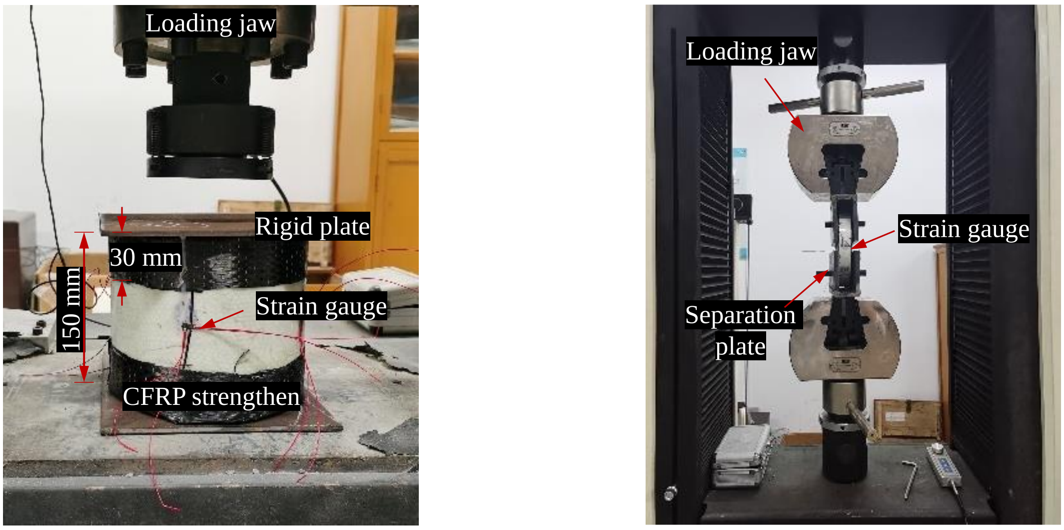

(a) Longitudinal compression (b) Hoop tension

Fig. 6. Mechanical test of FRP tube.

The uniaxial tensile test for Q235 steel was conducted in accordance with the Chinese code GB/T 228-2021 [43]. The measured yield strength and ultimate strength are 258 MPa and 435 MPa, respectively, while the elastic modulus is 202 GPa.

3 Experimental programs

3.1 Specimen design

Here, four UHPC-FFT composite columns, one Normal Strength Concrete-filled FRP Tube (NSC-FFT) and one UHPC-filled steel tube (UHPC-FST) composite column were designed and fabricated. The details of the specimens are illustrated in Fig. 7, and Table 4 shows the designed parameters of all specimens. All column sections have a diameter of 184 mm, a total height of 2100 mm, an effective height of 1500 mm. The longitudinal bars have a diameter of 12 mm, while the stirrups have a diameter of 6 mm and were spaced at intervals of 100 mm. All stirrups are fabricated from HRB400 grade steel. The FRP tubes were manufactured using a prefabricated filament winding method, with fiber winding direction at ±80°. Both the steel tube and FRP tube have a thickness of 4.0 mm, each. Both the top loading and the bottom foundation beams of column specimens are made of ordinary concrete, with densified reinforcement in the cross-section. The axial compression ratio n_c is defined by Eq. (4), where N represents the designed axial compressive load; f_c and A_c represent the compressive strength and cross-sectional area of concrete, respectively. Since the tubes are mainly used for confining concrete and the influence of longitudinal bars on the compressive load capacity of the specimen is minimal, the direct contribution of tubes and longitudinal bars to the axial load is neglected [44].

$$n_c = N / f_c A_c \tag{4}$$

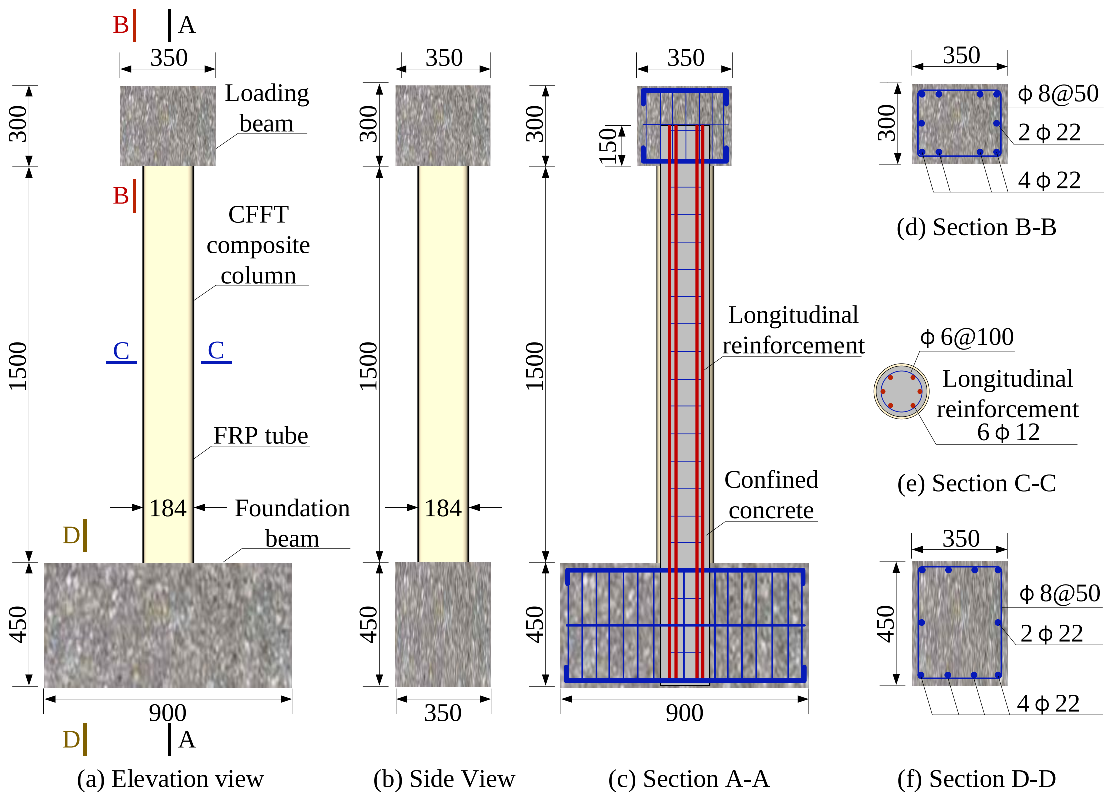

Fig. 7. Dimension and configuration of the specimen (unit: mm).

Table 4. Designed parameters of specimens.

No.	Concrete	Tube	t_f/mm	A_s	n_c
S1	UHPC	FRP	4.0	6ϕ S12	0.15

S2	UHPC	FRP	4.0	$6\phi^{B}12$	0.15
S3	UHPC	FRP	4.0	$6\phi^{H}12$	0.15
S4	UHPC	FRP	4.0	$6\phi^{S}12$	0.25
S5	UHPC	Q235 steel	4.0	$6\phi^{S}12$	0.15
S6	C40	FRP	4.0	$6\phi^{S}12$	0.15

Note: The superscripts "S", "H" and "B" attached to the symbol " ϕ " represent SFCB, HRB400-graded steel bar, and BFRP bar, respectively.

3.2 Specimen fabrication

The fabrication process for all composite columns is shown in Fig. 8. Firstly, the longitudinal and tie bars are polished at the measurement points until smooth, then cleaned with alcohol before attaching strain gauges. After installing the strain gauges on the bars, they are coated with sealant and then epoxy resin to reduce impact with the concrete slurry. Once the reinforcing bars are tied, they are placed into the wooden formwork of the foundation beam and concrete is poured. After seven days of curing with water, concrete is poured into the FRP tubes inside the foundation beam, followed by pouring the loading beam. Due to the strong fluidity of UHPC, the joints of the formwork need to be carefully inspected before pouring, and foam adhesive is used to seal any gaps to prevent slurry leakage. The molds are removed after two weeks of casting, followed by 28 days of natural curing.

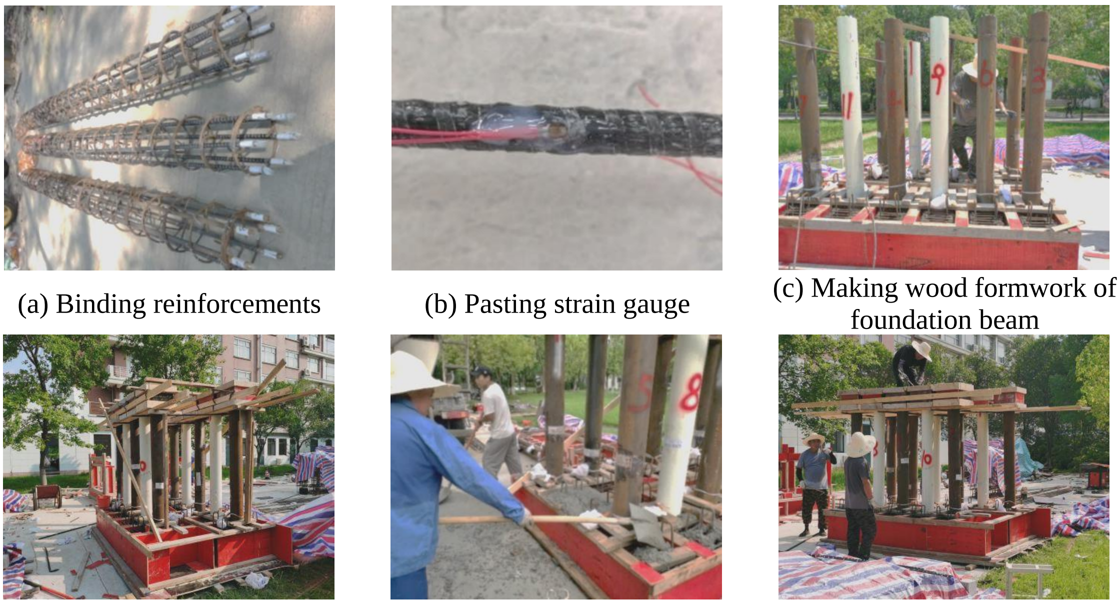

(a) Binding reinforcements (b) Pasting strain gauge (c) Making wood formwork of foundation beam

(d) Making wood formwork of loading beam (e) Pouring concrete of foundation beam (f) Pouring concrete of column

Fig. 8. Manufacturing process of composite columns.

3.3 Test setup and loading scheme

The loading device and test setup for test specimens are depicted in Fig. 9. During the testing process, vertical axial compression is applied by a hydraulic jack with a maximum load capacity of 1000 kN, and load sensors calibrated in advance are used for data acquisition. Throughout the entire process, a pulley system ensures that the hydraulic jack at the column top maintains vertical application of the vertical load. Horizontal loads are collected by sensors on the MTS hydraulic servo actuator, and horizontal displacement is measured by laser displacement sensors installed at the loading point (i.e., the geometric center of the column head). The foundation beam of the specimens is anchored to a rigid ground using anchor bolts, and horizontal displacement of the foundation beam is restricted by connecting it to a reaction wall via restraining steel plates and anchor bars.

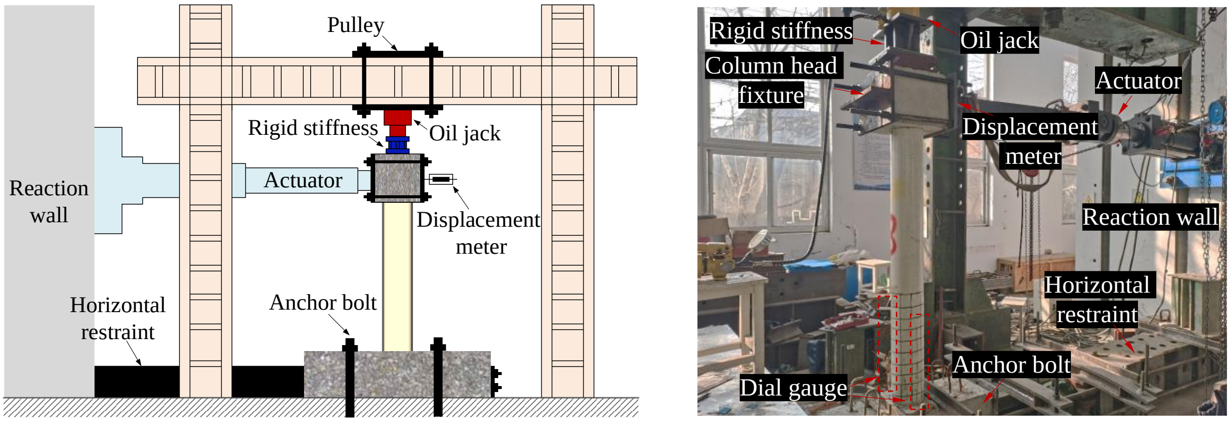

(a) Schematic (b) Photograph

Fig. 9. Schematic and photograph of test setup.

The layout of the strain gauges for tube and reinforcements is exhibited in Fig. 10. The strain gauges of reinforcements and FRP tube are distributed along the height direction at the plastic hinge region. Besides, the strain gauges of tube are placed longitudinally and circumferentially at the height of 50 mm, 200 mm and 350 mm, respectively. According to the Chinese code JGJ/T 101-2015 [45], the composite columns were initially subjected to a vertical axial pressure, maintaining the vertical load constant, before applying horizontal cyclic loading. The vertical axial pressure loading involves initial pre-loading, followed by meticulous monitoring of both the test instruments and specimens. Only after confirming the absence of any issues, full loading is applied. The horizontal loading system adopts full displacement control. When the drift ratio θ, that is the ratio of horizontal displacement to the effective height of the column, is less than 3.0%, the drift ratio is increased by 0.05% per level, with each level undergoing two cycles of reciprocating motion. When the θ is more than 3.0%, the drift ratio is increased by 1.0% per level [46], with each level undergoing one cycle of reciprocating motion. The loading is terminated when the horizontal load decreases to 85% of the peak load or when severe damage occurs to the test specimen. The specific loading protocol for horizontal loading is depicted in Fig. 11.

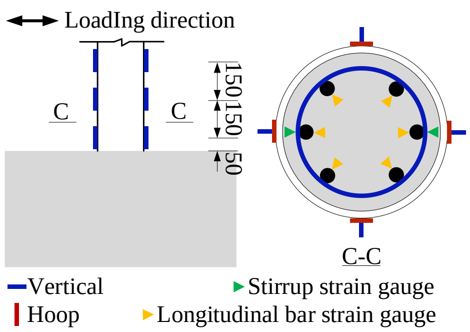

Fig. 10. Strain gauges for tube and reinforcements.

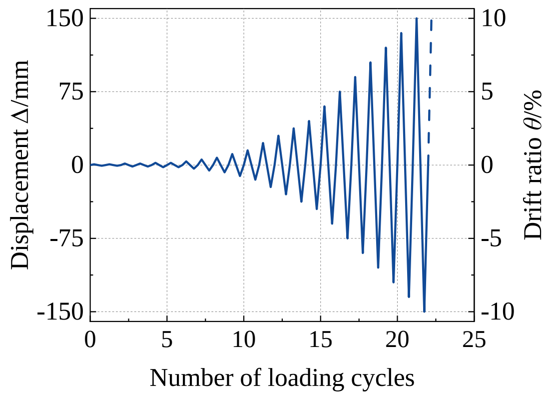

Fig. 11. Lateral cycling loading protocol.

4 Test results and discussion

4.1 Failure mode

In this experiment, all the composite columns experienced flexural failure. For convenience of discussion, the failure phenomena are categorized into two types based on the structural form.

4.1.1 Concrete-filled FRP tube composite column

The failure patterns of UHPC-FFT composite columns were generally similar, so the detailed discussion here is focused on specimen S1, as shown in Fig. 12. During the test, once the axial pressure was applied, the axial strain gauges on the FRP tube displayed noticeable readings, while the circumferential strain gauges showed relatively low readings. When the drift ratio θ < 0.9%, the test specimen remained in an elastic working state with no significant signs of damage. When θ = 0.9%, the internal longitudinal reinforcements started to yield, the concrete at the base of the column reached peak compressive strain, and localized cracks appeared in the FRP tube's base, exhibiting a lateral pattern. When θ = 2.4%, specimen transitioned into the elastic-plastic state with its load-bearing capacity reaching its peak, while the width of the transverse cracks at the FRP base increased, and the cracks extended significantly in length. When θ = 5.1%, the UHPC at the bottom of column began to crush to varying degrees, and the horizontal load dropped to about 85% of the peak load. At the same time, the FRP base showed multiple cracks due to the expansion caused by the crushing concrete, accompanied by persistent tearing noises. When θ = 5.6%, the load-bearing capacity sharply decreased, resulting in complete tearing at the bottom of the FRP tube, signifying the total failure of specimen.

The failure phenomena indicated that the severity of internal UHPC crushing increases with a higher axial load ratio of the composite columns. Compared with composite columns filled with NSC, those filled with UHPC exhibited significantly reduced concrete crushing, indicating that UHPC can effectively reduce damage under cyclic loading and improve seismic performance. Strain gauge readings showed that the FRP tube's highest circumferential strain occurred at 50 mm from the top of the column base. This is because the concrete at the column base, under maximum compression, expands the most, resulting in the highest circumferential strain in the FRP tube. At the end of the test, circumferential cracks in the FRP tubes of all specimens were mainly concentrated in the 0–300 mm height range at the base of the column, with no circumferential rupture observed.

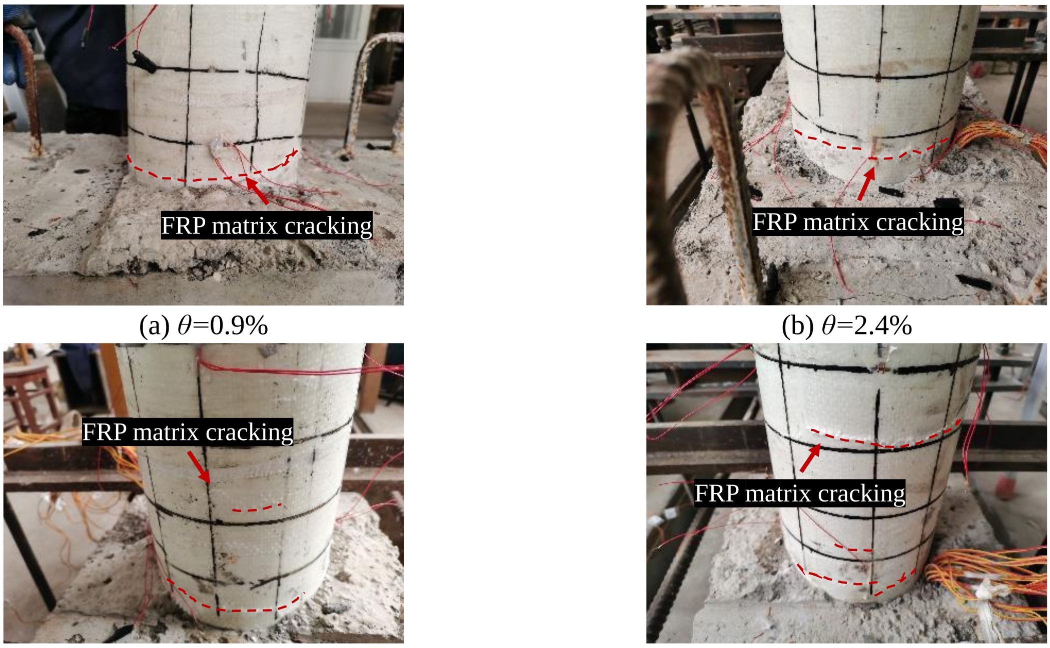

(a) θ=0.9% (b) θ=2.4%

(c) θ=5.1% (d) θ=5.6%

Fig. 12. Failure patterns of UHPC-FFT composite column (specimen S1).

4.1.2 Concrete-filled steel tube composite column

Figure 13 illustrates the failure pattern of the UHPC-FST composite column, specimen S5. When $\theta < 1.2\%$, the specimen operated in an elastic state with no significant signs of damage. At $\theta = 1.2\%$, the steel tube at the bottom of the specimen experienced local buckling, with slight outward bulging on the surface. As the displacement angle increased to $\theta = 2.1\%$, the specimen transitioned into a partial plastic state, reaching its peak load capacity, and the bulging at the steel tube base intensified, taking on a barrel-like shape. At $\theta = 7.1\%$, the UHPC at the base suffered severe crushing, causing the steel tube's bulging to extend circumferentially and resemble an elephant's leg. When $\theta = 7.6\%$, the load-bearing capacity sharply decreased, the steel tube at the column base underwent severe inward deformation, and specimen experienced complete failure.

(a) θ=1.2% (b) θ=2.1%

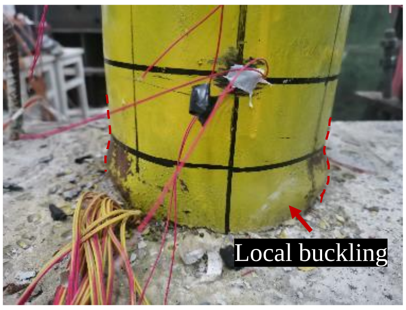

(c) θ=7.1%

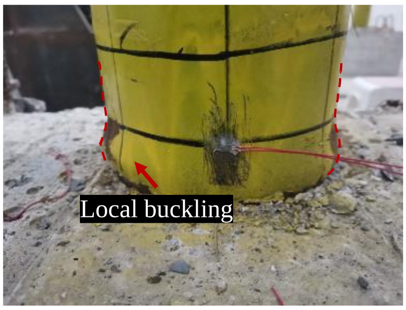

(d) θ=7.6%

Fig. 13. Failure patterns of UHPC-FST composite column (specimen S5).

4.2 Hysteretic curve

Figure 14 displays the hysteresis curves for all specimens. Where, "Exp" and "FE" refer to experimental and FEM results, respectively. The FEM hysteresis curves are obtained from the validated FE model as explained below. The hysteresis curves for all UHPC-FFT composite columns exhibit pronounced pinching, generally forming a double-flag shape. In contrast, the hysteresis curve for UHPC-FST composite column is more robust and spindle-shaped, with each hysteresis loop enclosing a larger area than that of FRP tube concrete composite columns, indicating a greater energy-dissipation capacity. This difference is due to steel tubes being elastoplastic materials with a much higher elastic modulus than the elastic-brittle FRP tubes, allowing steel tubes to enhance the lateral strength and plastic deformation capacity of composite columns, thus contributing more effectively to energy dissipation.

For the same axial compression ratio, the BFRP-UHPC-FFT composite column exhibited the most significant pinching in their hysteresis curves, followed by SFCB-UHPC-FFT composite columns, with the steel-reinforced UHPC-FFT composite column showing the least pinching. The pinching characteristics of the hysteresis curves are mainly influenced by the recovery stiffness during unloading. Since BFRP bars have the lowest initial elastic modulus and lack secondary stiffness, they exhibit minimal recovery stiffness when not ruptured, resulting in the most significant pinching. In contrast, steel bars have the highest initial elastic modulus with almost negligible secondary stiffness, providing relatively high recovery stiffness during unloading. SFCB has an intermediate initial elastic modulus with noticeable secondary stiffness, leading to intermediate recovery stiffness and moderate pinching in the hysteresis curves. Comparing the overall hysteresis curves, SFCB-UHPC-FFT composite columns demonstrate the fullest curves and the best hysteresis performance, while BFRP-UHPC-FFT composite column has the least full curves and the weakest hysteresis performance.

As the axial compression ratio increased from 0.15 to 0.25, the shape of the UHPC-FFT composite columns' hysteresis loops changed significantly, with an increase in load capacity but faster degradation, resulting in premature concrete crushing and reduced final deformation. For the same axial compression ratio, using UHPC instead of NSC can effectively enhance the energy dissipation performance of composite columns.

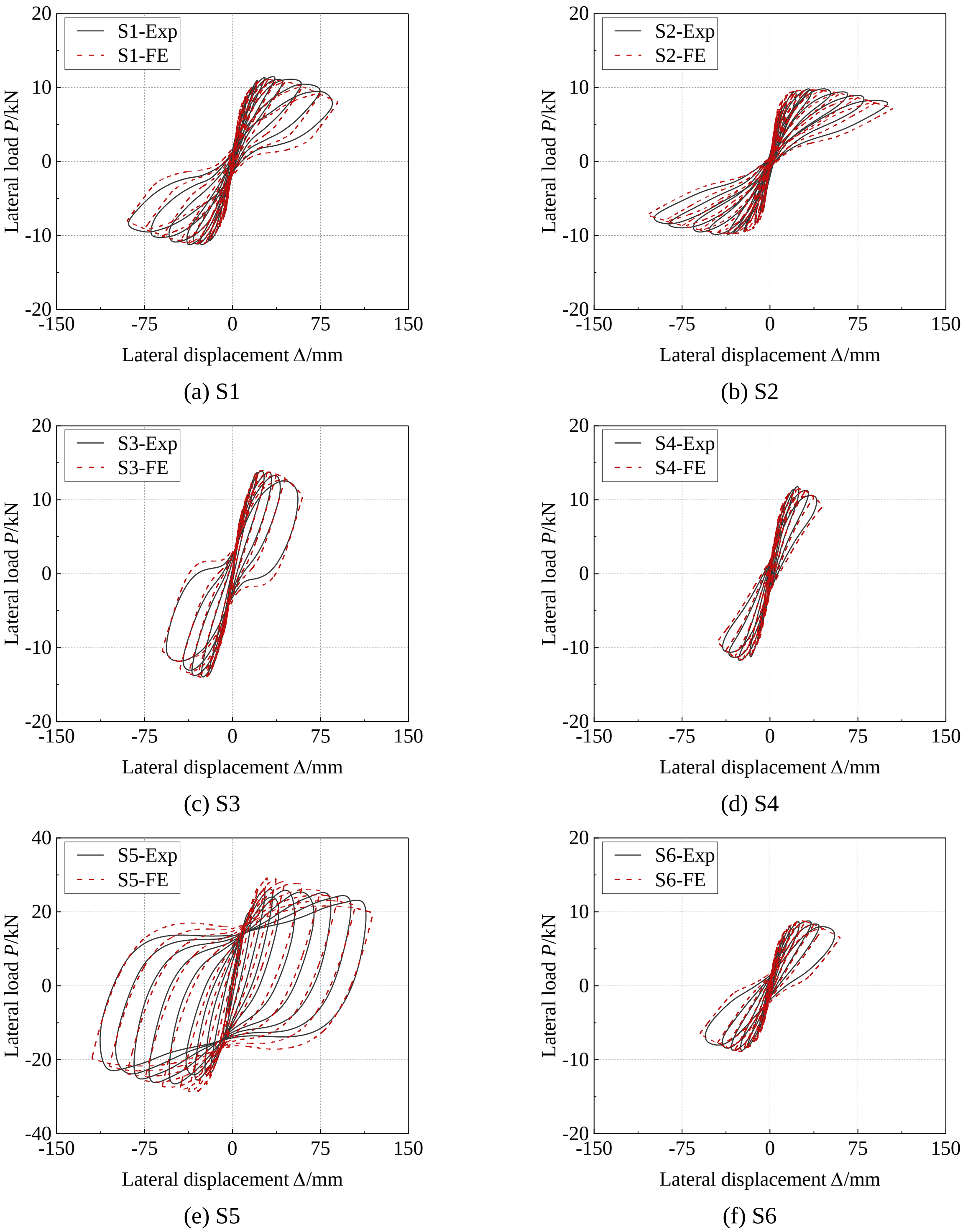

Fig. 14. Hysteretic curves.

4.3 Skeleton curve

Figure 15 shows the skeleton curves for each specimen, while Table 5 provides the characteristic loads, displacements, and ductility coefficients for the specimens. P_y, P_p, and P_u (P_u = 0.85 P_p) represent the yield, peak, and ultimate loads, respectively. Δ_y, Δ_p, and Δ_u are the corresponding horizontal displacements. The displacement ductility coefficient μ_Δ is the ratio of the ultimate displacement to the yield displacement. Characteristic loads and displacements for each specimen are averaged from the absolute values in the positive and negative loading directions. The yield points were determined using the equal-energy method [47].

The skeleton curves of all the composite columns exhibit an S-shape, characterized by three distinct stages, namely elastic, elastoplastic strengthening, and softening. The characteristic load of the BFRP-UHPC-FFT composite column is the lowest, followed by the SFCB-UHPC-FFT composite columns, with the steel-reinforced UHPC-FFT composite column having the highest. The deformation, however, exhibits an inverse trend, with the BFRP-UHPC-FFT composite column displaying the least amount of deformation and the steel-reinforced UHPC-FFT composite column exhibiting the highest level, while the SFCB-UHPC-FFT composite columns fall in between. Due to the fact that the steel bar has the highest elastic modulus but the lowest post-yield stiffness ratio (the ratio of post-yield stiffness to elastic modulus), while the BFRP bar has the lowest elastic modulus and shows no yield behavior, and SFCB falls in between both in terms of elastic modulus and post-yield stiffness, this leads to different performance characteristics for composite columns. Composite columns reinforced with steel bars have the highest initial stiffness but also the fastest stiffness degradation rate, and they exhibit the greatest deformation at failure. In contrast, composite columns reinforced with BFRP bars have the lowest initial stiffness but the slowest stiffness degradation rate, and they also exhibit the greatest deformation at failure. Composite columns reinforced with SFCBs exhibit initial stiffness and stiffness degradation rates that are between those of steel bars and BFRP bars, and their deformation at failure is also intermediate. Therefore, the deformation capacity of composite columns is influenced not only by the elastic modulus of the reinforcement but also by the post-yield stiffness.

As the axial compression ratio increases from 0.15 to 0.25, the yield, peak, and ultimate loads increase by 15.8%, 4.39%, and 5.26%, respectively, while peak and ultimate displacements significantly decrease. This is due to the more pronounced P-Δ second-order effect in the composite column under higher axial load ratios, which increases the risk of buckling, causes earlier cracking of FRP tubes, and significantly reduces the FRP's confinement on UHPC, while exacerbating damage to UHPC. Additionally, because of the high compressive strength of UHPC and the relatively low elastic modulus of the FRP tube, the confinement effect of FRP on UHPC is limited. Consequently, the increase in horizontal load-bearing capacity is minimal. This phenomenon also consistent with Feng et al.'s findings [48]. Besides, greater axial pressure also results in larger initial compressive strains for UHPC. Under cyclic loading, the increased cumulative plastic deformation accelerates the damage rate in UHPC, leading to a faster degradation in load-bearing capacity. Comparing UHPC-FFT composite columns with UHPC-FST composite columns, the UHPC-FST composite column exhibit significantly stronger load-bearing capacity and deformation capability compared with UHPC-FFT composite columns.

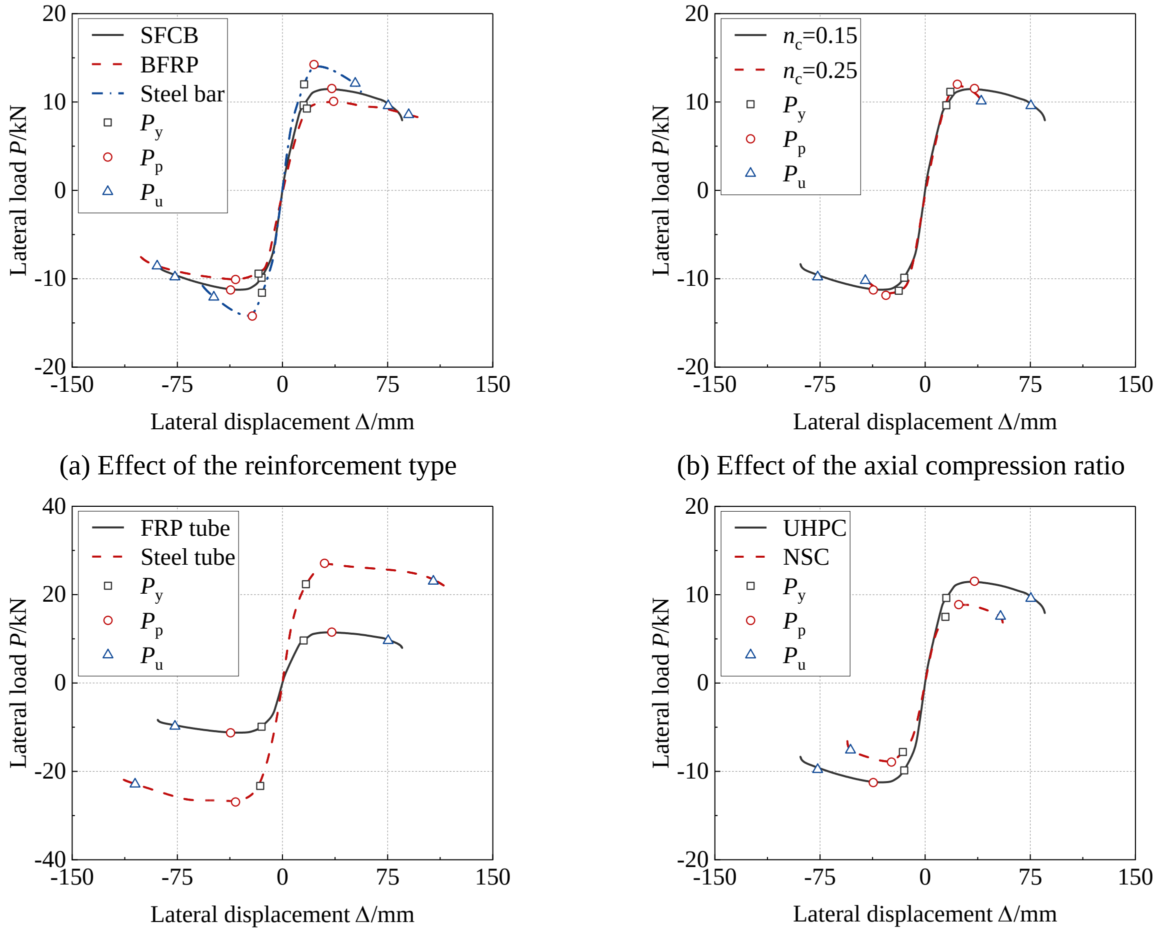

(a) Effect of the reinforcement type

(b) Effect of the axial compression ratio

(c) Effect of the tube type

(d) Effect of the concrete type

Fig. 15. Skeleton curves.

Table 5. Details of the experimental results.

Specimen	Direction	P_y (kN)	Δ_y (mm)	P_p (kN)	Δ_p (mm)	P_u (kN)	Δ_u (mm)	μ_Δ
S1	Positive	9.63	15.1	11.5	35.2	9.58	75.4	5.00
	Reverse	-9.89	-14.9	-11.3	-37.0	-9.80	-76.7	5.13
	Average	9.76	15.0	1.4	36.1	9.69	76.0	5.06
S2	Positive	9.26	17.4	10.1	36.5	8.56	90.0	5.16
	Reverse	-9.42	-17.1	-10.1	-33.5	-8.57	-89.4	5.23
	Average	9.34	17.3	10.1	35.0	8.56	89.7	5.19
S3	Positive	12.0	15.4	14.2	22.5	12.1	51.9	3.37
	Reverse	-11.6	-14.7	-14.2	-21.5	-12.1	-49.0	3.34
	Average	11.8	15.0	14.2	22.0	12.1	50.4	3.36
S4	Positive	11.1	17.9	12.0	22.9	10.1	40.0	2.23
	Reverse	-11.4	-18.8	-11.9	-28.0	-10.2	-42.7	2.27
	Average	11.3	18.4	11.9	25.5	10.2	41.3	2.25
S5	Positive	22.3	16.8	27.1	30.0	23.0	108	6.42
	Reverse	-23.3	-15.9	-26.9	-33.5	-22.9	-105	6.63
	Average	22.8	16.3	27.0	31.8	23.0	106	6.52
S6	Positive	7.49	14.4	8.88	23.9	7.55	53.8	3.73
	Reverse	-7.80	-15.9	-8.94	-24.0	-7.60	-53.3	3.35

Average	7.65	15.2	8.91	24.0	7.57	53.5	3.53

Note: "Average" represents the mean of the absolute values in two loading directions.

4.4 Strain response

To illustrate the relationship between longitudinal reinforcement strain and load, this section analyzes the strain-horizontal load curves for typical specimens, as shown in Fig. 16. The longitudinal reinforcement in specimens S1, S3, and S5 has yielded by the time the load reaches its peak value. When the bearing capacity reaches the ultimate load, the plastic strain of the longitudinal reinforcement is relatively large, especially the longitudinal reinforcement of specimen S5 is close to the rupture strain. This suggests that, with an axial compression ratio of 0.15, the deformation between the longitudinal reinforcement and UHPC in composite columns is well-coordinated, and the tensile strength of reinforcement is fully utilized. Specimen S5 (UHPC-FST composite column) achieves the highest utilization of the tensile performance of the longitudinal reinforcement. However, specimen S4, with a high axial compression ratio, reaches the peak load before SFCB has yielded, and even when the load reaches the ultimate value, it still retains significant deformation capacity. This indicates that when the axial compression ratio is too high, composite columns cannot fully utilize the superior tensile properties of SFCB, leading to inefficient of the material.

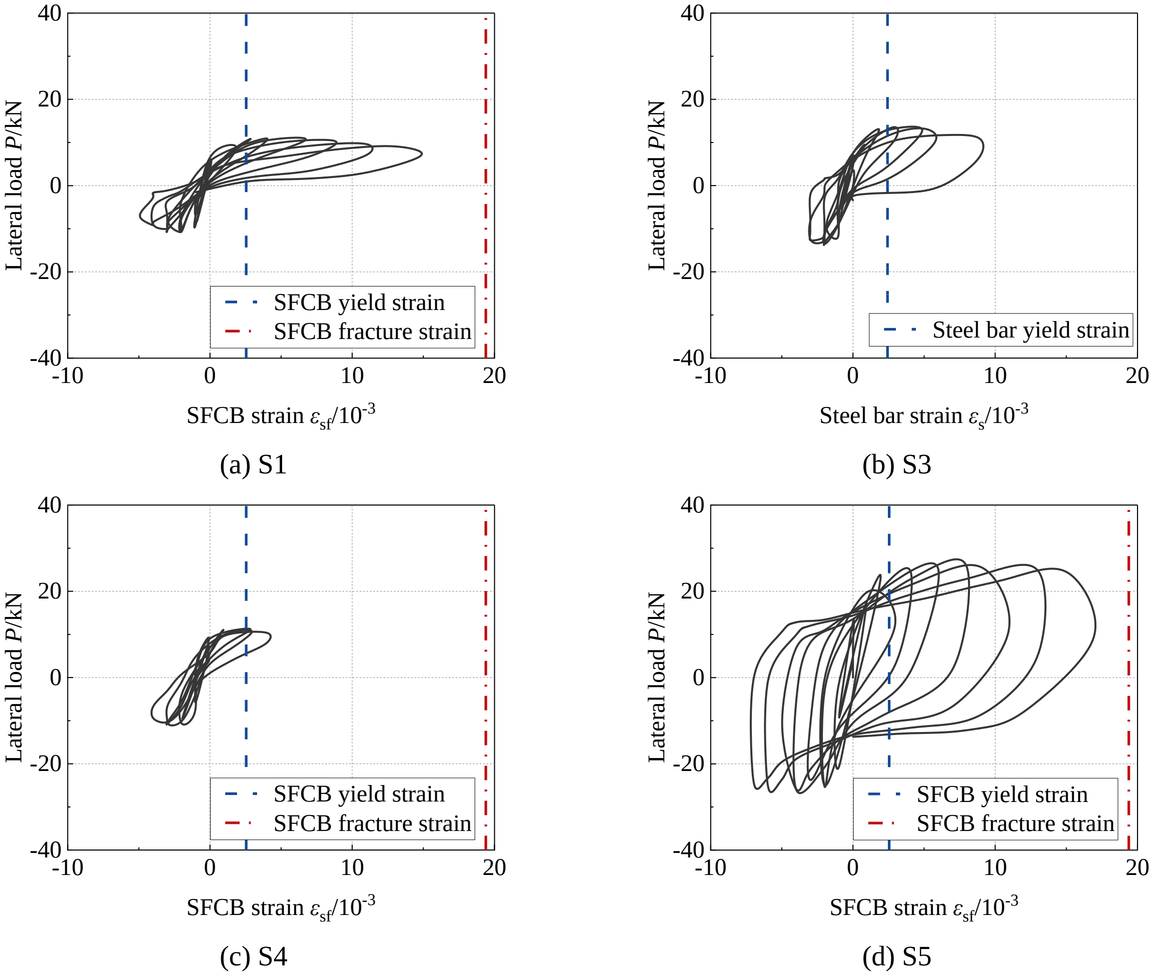

Fig. 16. Longitudinal bar strain-lateral load curves.

5 Seismic performance analysis

5.1 Ductility

The displacement ductility coefficient μ_Δ, defined as the ratio of the ultimate displacement Δ_u to the yield displacement Δ_y, reflects the ductility characteristics of composite columns, as shown in Eq. (5).

$$\mu = \Delta_u / \Delta_y \tag{5}$$

Table 5 lists the displacement ductility coefficients for all specimens, with values representing the average of the absolute values from both positive and negative loading directions. SFCB-UHPC-FFT composite columns exhibit the highest ductility, while the steel bar-reinforced UHPC-FFT composite column shows the least, with BFRP-UHPC-FFT composite column falling in between. This is because SFCB has an initial elastic modulus between BFRP and steel, but the highest secondary stiffness. This feature allows the plastic hinge region at the base of the column to maintain good resistance to bending moments after SFCB yields. However, in steel bar-UHPC-FFT composite column, once the steel bars yield, the moment resistance in the plastic hinge region no longer increases. The crushing of the core concrete intensifies, leading to an accelerated rate of load-bearing capacity degradation. Compared with SFCB-UHPC-FFT composite columns, the steel bar-UHPC-FFT composite column exhibits smaller displacements at both peak and ultimate loads, but demonstrates poorer ductility. The composite columns with an axial compression ratio of 0.15 exhibit 2.25 times the ductility compared with those with an axial compression ratio of 0.25, indicating that higher axial compression ratios result in poorer ductility. Replacing NSC with UHPC, or using steel tubes instead of FRP tubes can improve the ductility of composite columns, with the most significant improvement in ductility observed when steel tubes are used to replace FRP tubes.

5.2 Stiffness degradation

The secant stiffness K_i is calculated from the formula presented in Eq. (6). Where P_i and Δ_i are the peak load and corresponding horizontal displacement at the i^{th} stage loading, respectively. + and - indicate the loading direction. The stiffness degradation curves of all specimens are shown in Fig. 17.

$$K_i = \frac{|+P_i| + |-P_i|}{|+\Delta_i| + |-\Delta_i|} \tag{6}$$

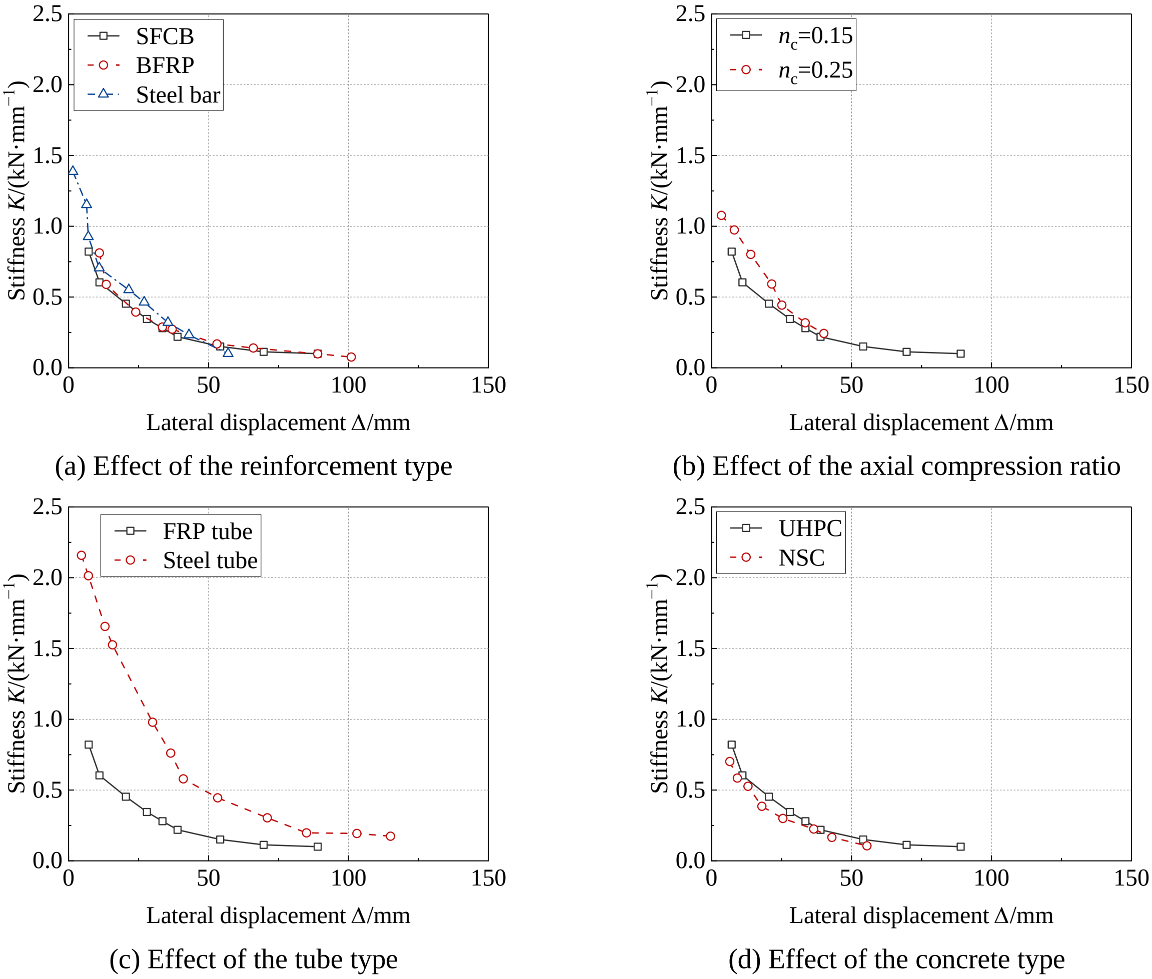

(a) Effect of the reinforcement type (b) Effect of the axial compression ratio

(c) Effect of the tube type (d) Effect of the concrete type

Fig. 17. Comparation of the stiffness degradation.

The stiffness of specimens generally decreases with increasing horizontal displacement, with a noticeable decline in stiffness at the beginning of the loading process. However, as the displacement increases, the rate of stiffness degradation tends to stabilize.

The steel bar-UHPC-FFT composite column has the highest initial stiffness, followed by SFCB-UHPC-FFT composite columns, while the BFRP-UHPC-FFT composite column exhibits the lowest stiffness. Besides, the rate of stiffness degradation is highest for the steel bar-reinforced column, then SFCB-reinforced columns, and lowest for the BFRP-reinforced column. This indicates that the initial stiffness of composite columns is positively correlated with the initial elastic modulus of the longitudinal reinforcement, while the rate of stiffness degradation is positively correlated with the secondary stiffness of the longitudinal reinforcement. This is because the secondary stiffness ratio of steel bars (the ratio of post-yield modulus to initial modulus) is the smallest, while that of BFRP is the largest (equal to 1.0), with SFCB falling in between. Consequently, BFRP-UHPC-FFT composite columns exhibit strong recovery capabilities, minimal cumulative damage to the core concrete under cyclic loads, and less degradation of load-bearing capacity. Therefore, the smaller the secondary stiffness ratio of the reinforcement, the lower the stiffness degradation rate of UHPC-FFT composite columns. Comparing the impact of the three reinforcement materials on stiffness degradation, SFCB offers a balance between high initial stiffness and improved stiffness degradation resistance.

Increasing the axial compression ratio can boost the initial stiffness of composite columns, but it also exacerbates stiffness degradation after peak load. This is because, as the axial compression ratio increases, concrete crushing in the plastic hinge zone becomes more severe, leading to a faster rate of performance degradation in the composite columns. UHPC-FST composite columns exhibit significantly higher initial stiffness, but their stiffness degradation rate is also quicker. As horizontal displacement increases, the UHPC inside the column base crushes and expands. However, steel tubes have a limited constraining effect on UHPC, and once the circumferential stress reaches the yield strength of the steel tube, the constraint effect does not increase further. Conversely, FRP tubes continually increase their constraint effect on UHPC until they rupture, thereby helping to delay stiffness degradation.

By comparing composite columns filled with different types of concrete, it can be observed that UHPC-FFT composite columns consistently exhibit greater stiffness than the NSC-FFT composite column at the same level of horizontal displacement. Additionally, the stiffness degradation rate of UHPC-FFT composite columns is slower. This is attributed to the higher packing density of UHPC compared with NSC and the bridging effect of steel fibers, which provide superior mechanical properties and result in less cumulative damage under cyclic loading, thereby enhancing recovery.

5.3 Energy dissipation

Cumulative energy dissipation, E, is utilized for evaluating the energy dissipation capacity of all test specimens, as depicted in Fig. 18. The cumulative energy dissipation can be determined by integrating the sum of the areas of all the individual hysteresis loops depicted within the hysteresis curves. The cumulative energy dissipation increases steadily with greater horizontal displacement. Comparing specimens with longitudinal reinforcement of SFCB, BFRP, and steel, the SFCB-UHPC-FFT composite columns exhibit the highest cumulative energy dissipation, while the BFRP-UHPC-FFT composite column has the lowest, with the steel-reinforced UHPC-FFT composite column falling in between. Although the number of hysteresis loops before failure is lower for SFCB-UHPC-FFT composite columns than for BFRP-UHPC-FFT composite columns, SFCB's superior secondary stiffness allows the SFCB-UHPC-FFT composite columns to dissipate significantly more energy at each loading level. Overall, this suggests that UHPC-FFT composite columns made with SFCB provide the best seismic performance compared with those with steel or BFRP bars.

Specimens with higher axial compression ratios have greater cumulative energy dissipation early in the loading process, but they eventually exhibit lower cumulative energy dissipation. This is because a higher axial compression ratio shortens the elastic phase, leading to an earlier transition into the plastic phase. In contrast, specimens with a lower axial compression ratio have an extended failure cycle, allowing for greater plastic energy dissipation. Using UHPC instead of NSC can significantly improve the cumulative energy dissipation of the specimens. The cumulative energy dissipation of UHPC-FST composite columns consistently surpasses that of UHPC-FFT composite columns, with the difference becoming more pronounced as horizontal displacement increases. This is because steel tube has a higher elastic modulus and exhibit significant yielding behavior, contributing more to energy dissipation during cyclic loading. Moreover, the steel tube did not exhibit local tearing during cyclic loading, providing stronger confinement to the UHPC. In contrast, FRP tubes experience matrix cracking during loading, which weakens their confinement of UHPC. Therefore, the hysteresis curve of UHPC-FFT composite columns is fuller, and its cumulative energy dissipation is greater.

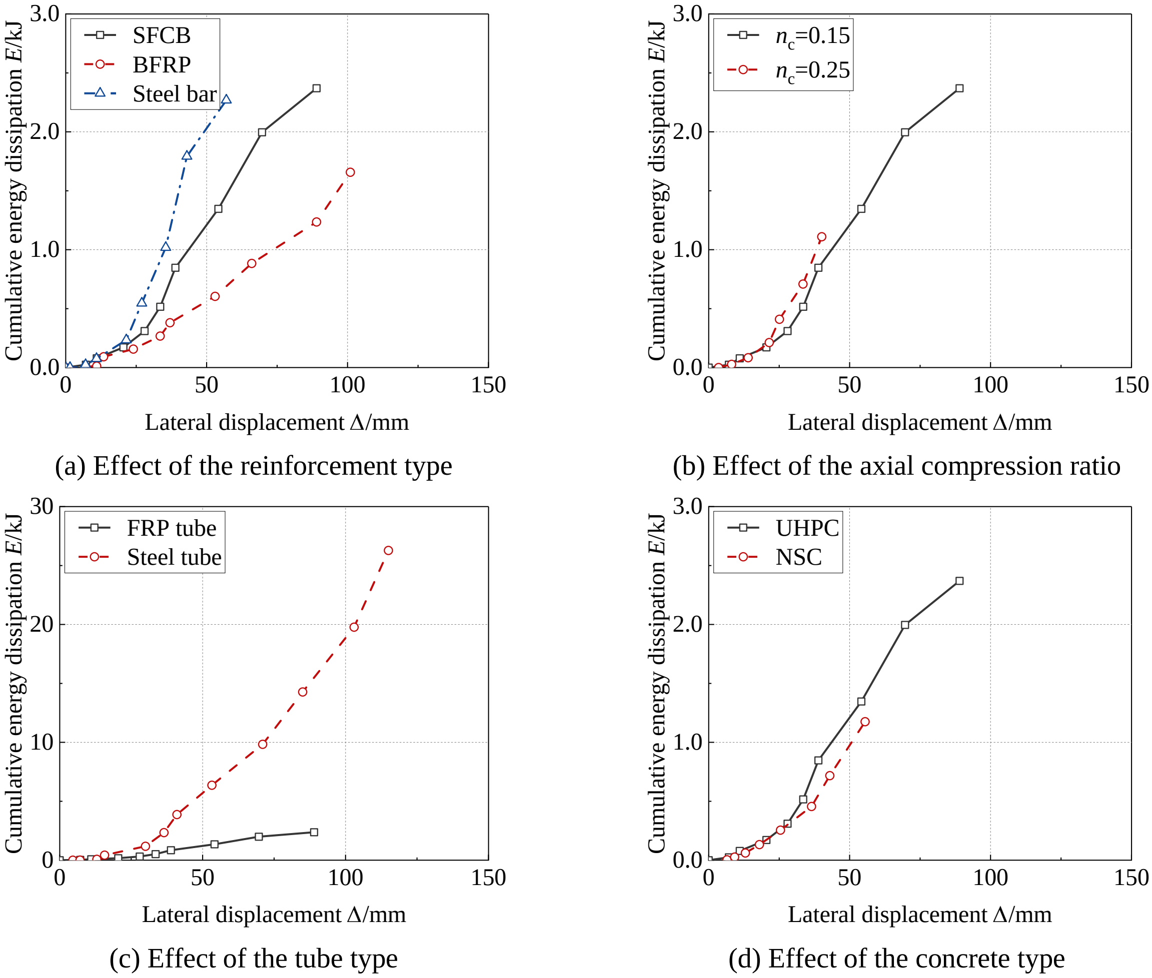

(a) Effect of the reinforcement type

(b) Effect of the axial compression ratio

(c) Effect of the tube type

(d) Effect of the concrete type

Fig. 18. Comparation of the cumulative energy dissipation.

5.4 Residual deformation

Residual deformation, Δ_r, is a crucial metric for assessing earthquake damage, post-earthquake structural functionality, and repair and strengthening requirements [13-14]. It is defined as the deformation of a specimen after being unloaded to a zero-horizontal load, following positive and negative loading. The ability of composite columns to return to their initial state after unloading the horizontal force is known as the self-resetting capability. The smaller the residual deformation of the composite columns, the stronger their self-resetting capability. Fig. 19 shows the residual deformation for all specimens.

Comparing specimens with longitudinal reinforcements of SFCB, BFRP, and steel bars, the steel bar-UHPC-FFT composite column exhibits the most residual deformation, while the BFRP-UHPC-FFT composite column has the least, with SFCB-UHPC-FFT composite columns in between. This suggests that residual deformation is positively correlated with the initial elastic modulus of the reinforcement. Residual deformation in steel-reinforced UHPC-FFT composite column increases rapidly when the displacement angle exceeds 2.0%, indicating that columnist has reached their peak load. As loading continues, the UHPC at the base of the column undergoes increasing crushing, causing deformation between the steel bar and UHPC to become misaligned, leading to a significant increase in residual deformation.

An increased axial compression ratio results in a noticeable increase in residual deformation. This occurs because higher axial compression ratios lead to more severe concrete crushing at the base for the same horizontal displacement, causing the composite columns to demonstrate the plastic phase earlier and weakening their self-resetting capability. The UHPC-FST composite column exhibits significantly greater residual deformation compared with UHPC-FFT composite columns, due to the steel tube's elastoplastic behavior, allowing for greater plastic deformation in the composite columns. Residual deformation in UHPC-FFT composite columns is much lower than in NSC-FFT composite column, owing to UHPC's stronger mechanical properties, which effectively delay the plastic hinge zone's failure at the column base, reducing the specimen's plastic deformation and significantly enhancing the self-resetting capability of the composite columns.

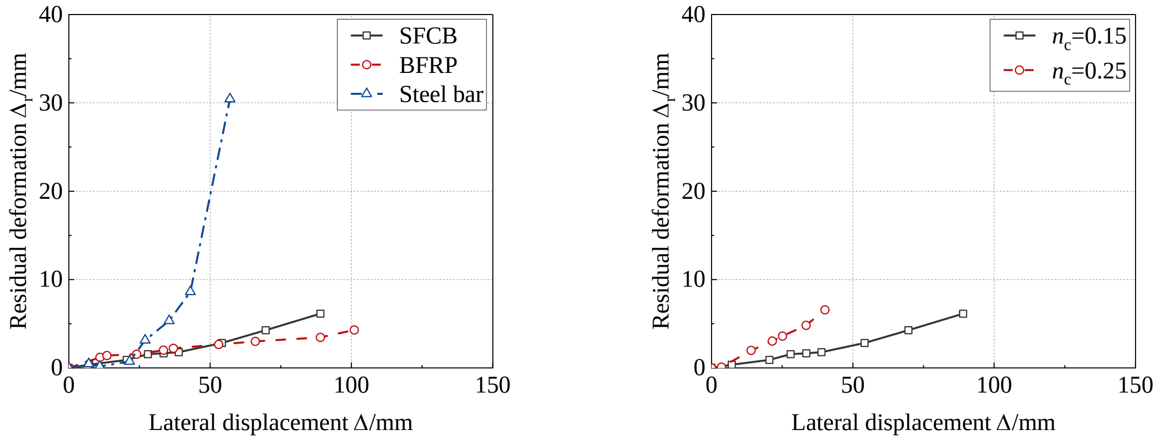

(a) Effect of the reinforcement type

(b) Effect of the axial compression ratio

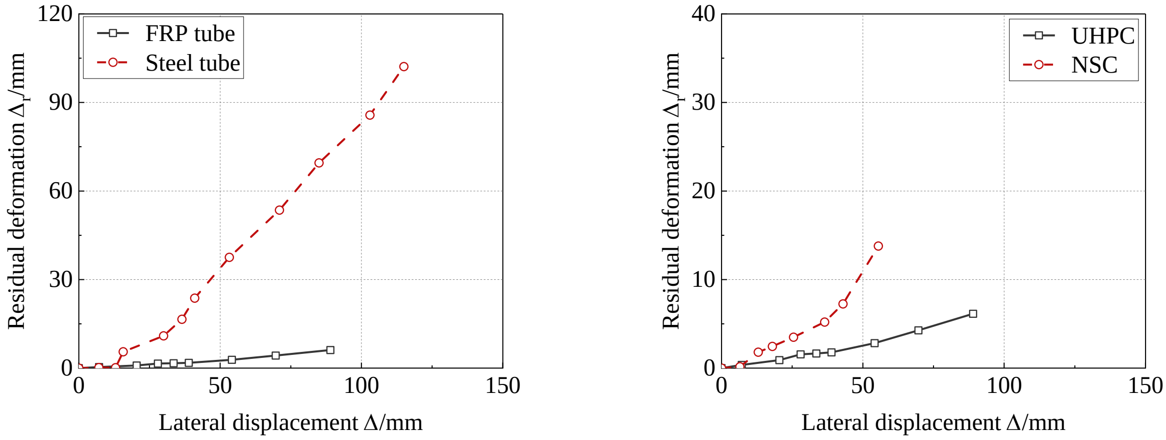

(c) Effect of the tube type (d) Effect of the concrete type

Fig. 19. Comparation of the residual deformation.

6 Finite element analysis

6.1 Establishment of FEM

The hysteresis analysis of UHPC-FFT composite columns is described in this section, utilizing FEMs developed in OpenSEES, based on the previously measured material properties. The "NonlinearBeamColumn" element, that consideres the development of plasticity and geometrical nonlinearity, was adopted to construct the FEM for UHPC-FFT columns. Based on a convergence study, five segments are identified along the height of the column to achieve an optimal balance between model accuracy and computational time efficiency. The column base is set as a fixed end, and torsional deformation is neglected. The specific boundary conditions and fiber element division are shown in Fig. 20.

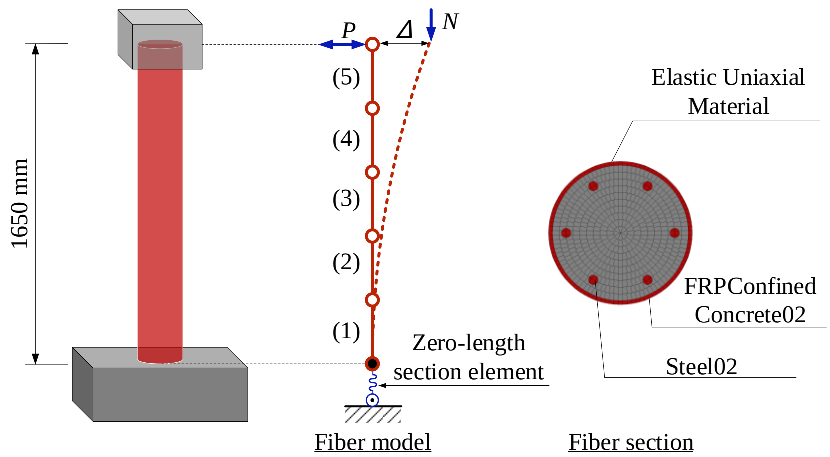

Fig. 20. Numerical model for SFCB-UHPC-FFT composite column.

6.2 Stress-strain models of materials

The internal concrete uses the "FRPConfinedConcrete02" model, derived from the work of Lam and Teng et al. [49-50], which simulate the cyclic compressive and tensile cyclic behavior of concrete, according to the model of Yassin [51] with some minor modifications. The model of Lam and Teng et al. [49-50] can provide fairly accurate stress-strain curves for CFFTs built with either ordinary or high-strength concrete. To construct the uniaxial hysteretic constitutive model, "FRPConfinedConcrete02" allows users to input basic parameters (such as the thickness of the FRP tube, Young's modulus, fracture strain, concrete section size, and the properties of ordinary unconfined concrete) or define limiting conditions (such as the peak stress and limit strain of confined concrete and the properties of ordinary unconfined concrete) [17-18].

The steel bars and SFCB use the "Steel02" model. The constitutive model, proposed by Menegotto and Pinto [52], uses an explicit function of strain, providing advantages such as good convergence and high computational efficiency. This model effectively captures the performance of reinforcement materials under cyclic loading. Due to the relatively small cross-sectional area of the reinforcement and its minimal compressive role in composite columns, SFCB is assumed to be a material with equal tensile and compressive strengths.

The BFRP bars and FRP tubes, both, utilize the "ElasticUniaxialMaterial" model. However, due to the one-dimensional nature of the fiber model, it fails to account for the anisotropic characteristics and biaxial stress state exhibited by FRP materials as represented in the "ElasticUniaxialMaterial" model. Thus, it also overlooks variations in confining stress across the cross-section of FRP tubes. Despite these aforementioned limitations, the current numerical model is generally capable of capturing the hysteresis behavior.

Zhao et al. [53] have found that end deformations caused by the strain penetration effect of longitudinal reinforcement at the base of columns can account for about 35% of the total deformation in bending members. To simulate this deformation component, a zero-length section element is used as shown in Fig. 20. The "Uniaxial-Material Bond_SP01" model, as proposed by Zhao et al. [53], incorporates the strain penetration effect of longitudinal reinforcement at the column base. This model is based on a large dataset from reinforced concrete pull-out tests and calculates the yield slip s_y, of the reinforcement as given by Eq. (7).

$$s_{\mathrm{y}} = 2.54\left(\frac{d_{\mathrm{s}}}{8437}\frac{f_{\mathrm{y}}}{\sqrt{f_{\mathrm{c}}'}}\left(2\alpha+1\right)\right)^{1/\alpha}+0.34 \tag{7}$$

Where d_{s} represent the diameter of the reinforcing bars; α is the local bond slip parameter, with a value of 0.4; f_{c}' is the compressive strength of concrete cylinder; and s_{u} is the ultimate slip (approximately 30~40 times s_{y}).

For the slip behavior of SFCB, which is covered with FRP and has stable secondary stiffness, its yield slip is expected to be greater than that of regular steel bars, making it inappropriate to directly apply Eq. (7). Currently, no researchers have studied the stress-slip relationship between SFCB and concrete, but Sun et al. [26] suggested setting the yield slip for SFCB to be 1.5 times that of regular steel bars. Further pull-out tests are needed to accurately determine the stress-slip relationship for SFCB. Since the "Uniaxial-Material Bond_SP01" model is suitable only for materials exhibiting yield behavior, the slip behavior of BFRP bar is not included when developing the finite element model for specimen S2.

6.3 Model validation

Figure 14 compares the hysteresis curves for all UHPC-FFT composite columns from both experimental and FEM results. The FEM analysis provides a reasonable representation of key performance indicators such as load-bearing capacity, stiffness, and deformation. While the finite element analysis tends to slightly overestimate the residual deformation under large deformations compared with the experimental results, the overall analysis results are in good agreement with the experimental data. In summary, the FEM developed here is accurate and can be used for further parametric analysis.

6.4 Parametrical analysis

Based on the validated FEM, a parametric study is conducted on SFCB reinforcing UHPC-FFT composite columns using push-over analysis. Specimen S1 is defined as the control specimen with the following characteristics: a sectional diameter of 184 mm, an FRP thickness of 4 mm, an effective height of 1500 mm, an axial compression ratio of 0.15, a diameter of 12 mm for SFCB, a steel reinforcement ratio of 0.71%, and a diameter and yield strength of the inner steel bar of 6 mm and 480 MPa, respectively. The elastic modulus and tensile strength of the outer-wrapped FRP are 47.3 GPa and 808 MPa, respectively. For each parameter analysis, only one parameter is altered at a time.

6.4.1 Slenderness ratio

Figure 21 shows the effect of slenderness ratio L/D (the ratio of effective height L to sectional diameter D) on the seismic performance of SFCB reinforcing UHPC-FFT composite columns. The initial stiffness and load-bearing capacity of composite columns increase significantly as the slenderness ratio decreases, while their deformation capacity is reduced. For slenderness ratios greater than or equal to 7.07, the failure mode of composite columns primarily involves the crushing of internal concrete, indicating a ductile failure behavior. Conversely, for slenderness ratios less than 7.07, the failure mode shifts to the fracture of SFCBs, exhibiting brittle failure characteristics. Therefore, when designing short columns with lower slenderness ratios, it is crucial to utilize SFCBs with greater fracture strain in order to prevent premature fracture under smaller deformations. To ensure the safe use of UHPC-FFT composite columns, it is recommended to use FEM and other analytical methods to optimize slenderness ratio during specimen design.

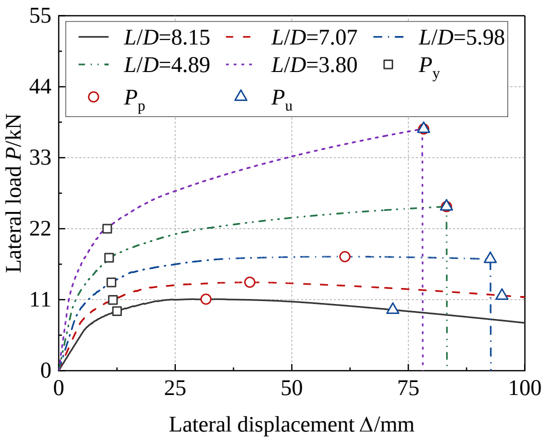

Fig. 21. Effect of slenderness ratio on load-displacement curves.

6.4.2 FRP tube's thickness

Figure 22 exhibits the effect of FRP tube's thickness t_f on the seismic performance of SFCB reinforcing UHPC-FFT composite columns. When the FRP tube thickness increases from 1 mm to 2 mm, the composite columns exhibit significant improvements in load-bearing capacity, deformation, and ductility, with a corresponding increase in initial stiffness and a noticeable reduction in stiffness degradation rate. However, when the FRP tube thickness exceeds 2 mm, the performance of the composite columns shows only slight improvement, confirming the optimum FRP tube thickness is around 2 mm. This is because the circumferential constraint effect of FRP tubes on UHPC has a limit. There is a threshold for FRP tube thickness, beyond which further increases do not significantly enhance the specimen's performance. If the FRP tube thickness is too large, it becomes uneconomical and has minimal impact. On the other hand, if it is too thin, it may not meet seismic requirements.

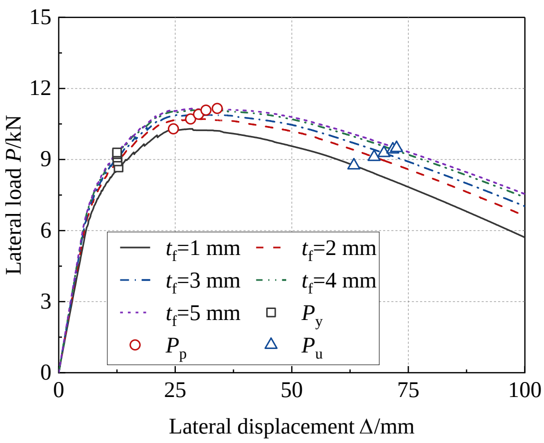

Fig. 22. Effect of SFCB's thickness on load-displacement curves.

6.4.3 SFCB's reinforcement ratio

Figure 23 shows the effect of SFCB's reinforcement ratio ρ_s on the seismic performance of SFCB reinforcing UHPC-FFT composite columns. When the reinforcement ratio of SFCB increases from

1.7% to 3.0%, the yield, peak, and ultimate load capacities, along with the corresponding displacements of the composite columns, significantly increase, leading to improved ductility. The initial stiffness of the horizontal load-displacement curve also increases, and the rate of stiffness degradation is delayed, with the failure mode consistently showing ductile failure. However, when the SFCB reinforcement ratio reaches 3.4%, the failure mode shifts from concrete crushing to SFCB rupture, indicating brittle failure. This occurs because the higher initial stiffness causes greater tensile strain in SFCB reinforcement when the concrete at the base of the column reaches its ultimate compressive strain. At the same horizontal displacement, the tensile strain in SFCB is greater, reaching its ultimate tensile strain earlier. Therefore, when the reinforcement ratio is high, it is necessary to use SFCB with a higher ultimate tensile strain.

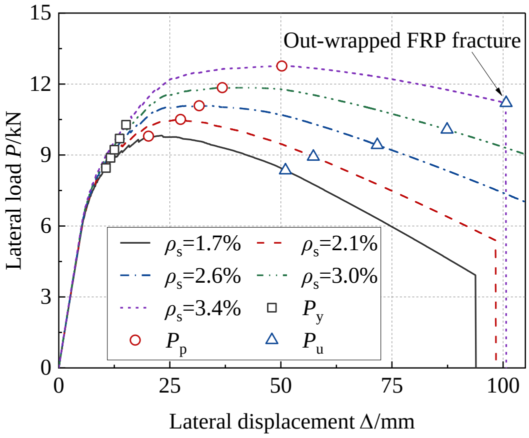

Fig. 23. Effect of SFCB's reinforcement ratio on load-displacement curves.

6.4.4 SFCB's sectional steel ratio

Figure 24 illustrates the effect of SFCB's sectional steel ratio a_s on the seismic performance of SFCB reinforcing UHPC-FFT composite columns. As the SFCB's sectional steel ratio increases, both the initial elastic modulus and yield strength of SFCB improve, resulting in a corresponding increase in the initial stiffness of the load-displacement curve and an increase in the yield, peak, and ultimate loads of the composite columns. The reduction in secondary stiffness and tensile strength, however, results in an increased rate of load degradation after reaching peak load. This leads to reductions in both peak and ultimate displacements, ultimately resulting in a significant decrease in ductility. The failure mode of composite columns consistently remains concrete crushing, indicating ductile failure. Thus, it is recommended to appropriately set the SFCB's sectional steel ratio to achieve an optimal balance between load-bearing capacity and ductility.

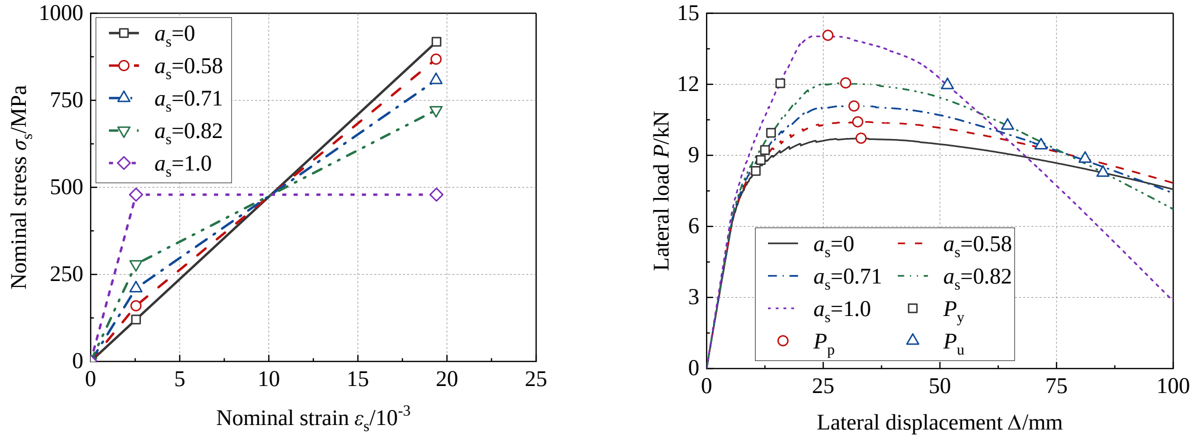

(a) Effect on SFCB's stress-strain curves (b) Effect on load-displacement curves

Fig. 24. Effect of SFCB's sectional steel ratio on seismic performance.

6.4.5 Yield strength of SFCB's steel bar

Figure 25 shows the effect of yield strength of SFCB's steel bar f_y on the seismic performance of SFCB reinforcing UHPC-FFT composite columns. With increasing yield strength of SFCB's steel bar, the initial elastic modulus of SFCB remains unchanged, but its yield strength improves, resulting in an increase in the yield, peak, and ultimate loads of the composite columns, without affecting the initial stiffness of the horizontal load-displacement curve of the composite columns. The secondary stiffness of SFCB remains constant, but its tensile strength increases, resulting in consistent load degradation rates after peak load and increased peak and ultimate displacements of the composite columns, with minimal change in ductility. The failure mode remains concrete crushing, indicating ductile failure. Thus, it is recommended to use higher-grade inner core steel to significantly improve the seismic performance of UHPC-FFT composite columns.

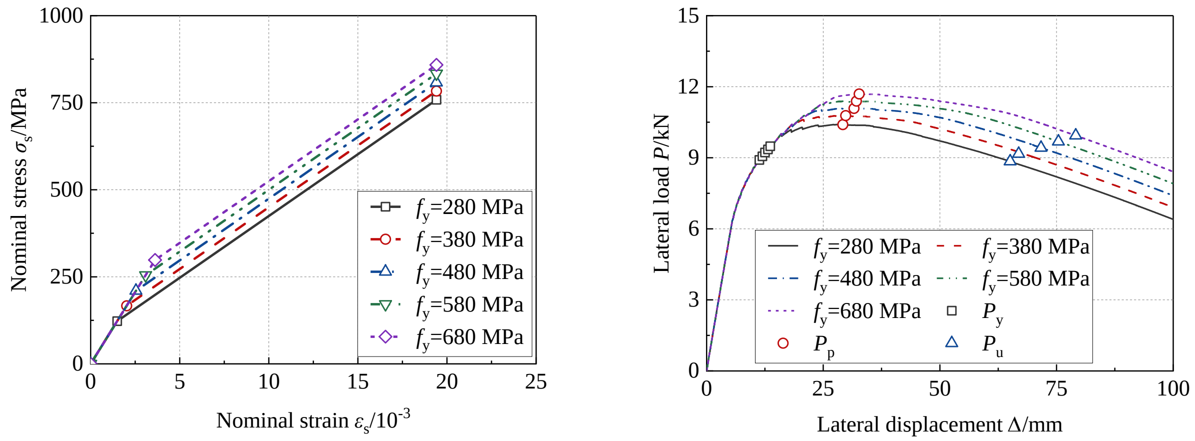

(a) Effect on SFCB's stress-strain curves (b) Effect on load-displacement curves

Fig. 25. Effect of SFCB's sectional steel ratio on seismic performance.

6.4.6 Elastic modulus of SFCB's out-wrapped FRP

Figure 26 exhibits the effect of elastic modulus of SFCB's out-wrapped FRP E_f on the seismic performance of SFCB reinforcing UHPC-FFT composite columns. As the effect of elastic modulus of SFCB's out-wrapped FRP increases, the initial elastic modulus and yield strength of SFCB improve, resulting in a corresponding increase in the initial stiffness of the load-displacement curve, and an increase in the yield, peak, and ultimate loads of the composite columns. With an increase in secondary stiffness and tensile strength but a reduction in ultimate tensile strain, the load degradation rate after peak load slows down, and the self-centering capability improves. When $E_f < 55$ GPa, both peak and ultimate displacements increase, leading to improved ductility; the failure mode remains concrete crushing. When $E_f \geq 55$ GPa, the peak displacement increases while the ultimate displacement decreases due to premature FRP failure, resulting in decreased ductility. The failure mode shifts to outer FRP rupture, leading to brittle failure. Therefore, it is recommended to set the elastic modulus of out-wrapped FRP at 55 GPa to achieve optimal seismic performance for composite columns.

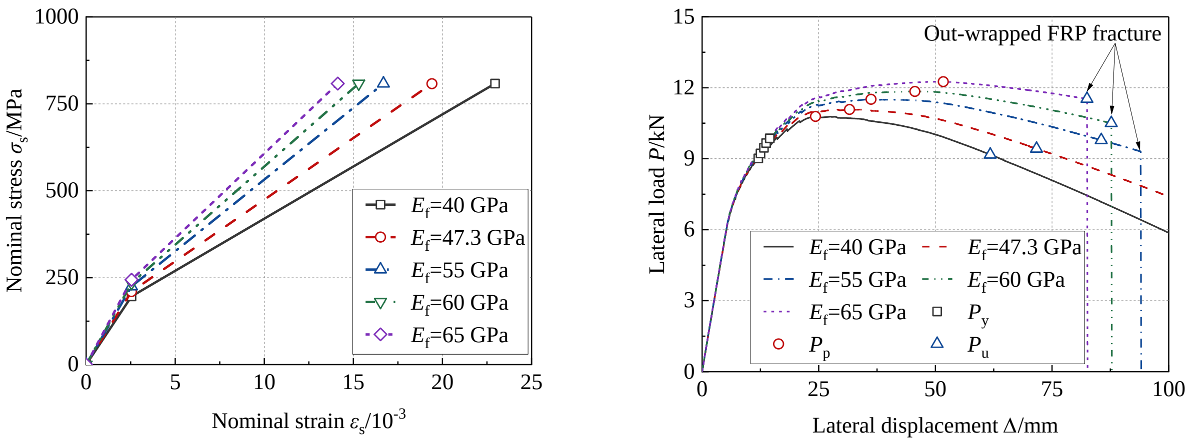

(a) Effect on SFCB's stress-strain curves (b) Effect on load-displacement curves

Fig. 26. Effect of elastic modulus of SFCB's out-wrapped FRP on seismic performance.

6.4.7 Tensile strength of SFCB's out-wrapped FRP

Figure 27 illustrates the effect of tensile strength of SFCB's out-wrapped FRP on the seismic performance of SFCB reinforcing UHPC-FFT composite columns. With an increase in the tensile strength of out-wrapped FRP, the initial elastic modulus and yield strength of SFCB do not change, indicating that the initial stiffness and load-bearing capacity of composite columns remain constant. The secondary stiffness of SFCB remains unchanged, leading to consistent load degradation rates after peak load. The ultimate load, displacement, and ductility of composite columns with an out-wrapped FRP's tensile strength of 300 MPa are comparatively lower due to the premature failure of the out-wrapped FRP. When the failure mode is the out-wrapped FRP rupture, lower tensile strength results in earlier failure of the SFCB, reducing the ultimate load and displacement. When the failure mode is concrete crushing, the tensile strength of the out-wrapped FRP has no impact on the seismic performance of composite columns.

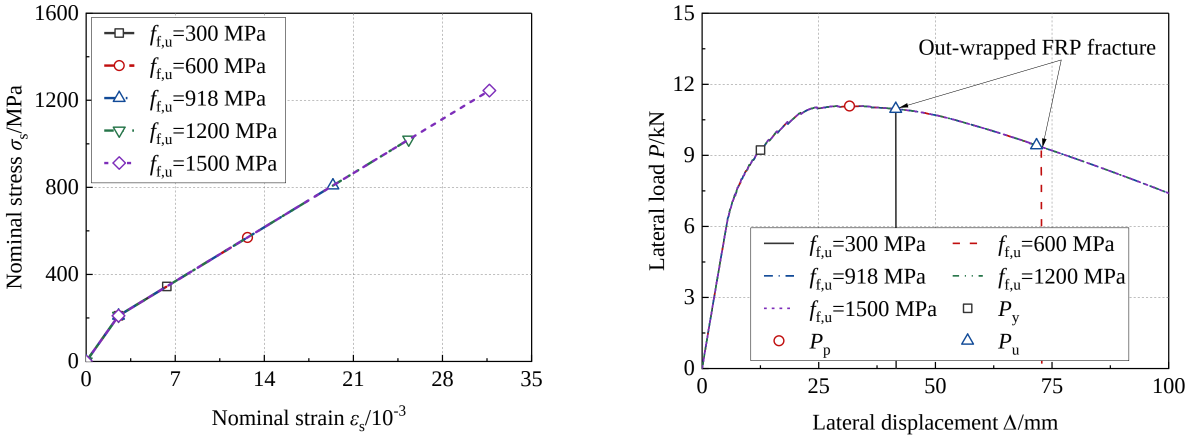

(a) Effect on SFCB's stress-strain curves (b) Effect on load-displacement curves

Fig. 27. Effect of SFCB's sectional steel ratio on seismic performance.

7 Conclusions

The seismic performance of SFCB reinforced UHPC-FFT composite columns were investigated through the pseudo-static tests and the FEM analysis. The main conclusions are summarized as follows.

(1) SFCB reinforced UHPC-FST composite columns demonstrate superior initial stiffness, load-bearing capacity, ductility, and energy dissipation compared with SFCB reinforced UHPC-FFT composite columns. However, the UHPC-FST composite column exhibits significantly greater residual deformation compared with UHPC-FFT composite columns. Furthermore, compared with steel or BFRP bars, SFCB can effectively reduce the residual deformation of composite columns.

(2) Increasing the axial compression ratio from 0.15 to 0.25 enhances load-bearing capacity of UHPC-FFT composite columns but reduces ductility and energy dissipation. Compared with NSC, filling UHPC can enhance the seismic performance of composite columns.

(3) Increasing the thickness of FRP tubes enhances the seismic performance of composite columns, but beyond a certain threshold, further thickness increments do not provide additional benefits. Increasing the reinforcement ratio of SFCB significantly improves the load-bearing capacity, deformation, and ductility of composite columns. However, excessively high reinforcement ratios may cause rupture of SFCB and shift the failure mode from ductile to brittle.

(4) Increasing the sectional steel ratio of SFCB effectively enhances initial stiffness and load-bearing capacity of composite columns, but accelerates stiffness degradation and reduces ductility. Increasing the yield strength of SFCB's steel core significantly improves load-bearing capacity and deformation capability without affecting ductility, initial stiffness, or the rate of stiffness degradation.

(5) The enhancement of elastic modulus of external FRP wrap enhances the load-bearing capacity, deformation characteristics, and ductility of composite columns. However, it may result in

premature failure caused by the outer-wrapped FRP rupture. It is recommended to set an elastic modulus for the outer FRP wrap at 55 GPa for optimal seismic performance in UHPC-FFT composite columns.

Although the SFCB reinforced UHPC-FFT composite columns proposed in this paper exhibit a significant lag behind steel tube concrete composite columns in terms of load-bearing capacity, deformation, and energy dissipation, they offer superior corrosion resistance and less residual deformation. Moreover, they demonstrate exceptional post-earthquake reparability. The primary research methods employed in this paper include quasi-static testing and one-dimensional fiber-modeling and future investigations aim to establish a restoring force model for the novel composite column, thereby providing theoretical support for its structural design and applications.

Conflict of interest

The authors declare that they have no known competing financial interests or personal relationships that could have appeared to influence the work reported in this paper.

Data Availability Statement

All data, models, or codes that support the findings of this study are available from the corresponding author upon reasonable request.

Acknowledgments

The authors would like to acknowledge the financial support from the High-End Foreign Experts Project of Ministry of Science and Technology, China (G2022014054L), the Natural Science Foundation of Jiangsu Province, China (BK20201436), the Science and Technology Cooperation Fund Project of Yangzhou City and Yangzhou University (YZ2022194), the Science and Technology Project of Jiangsu Construction System (2023ZD104 and 2023ZD105) and the Science and Technology Project of Yangzhou Construction System (202309 and 202312), Graduate Research and Innovation Projects of Jiangsu Province (KYCX24_3750), Jiangsu Provincial Government Scholarship for Studying Abroad (2024), Excellent Doctoral Dissertation Fund of Yangzhou University (2024).

References

[1] Zhou H J, Chen S Y, Du Y L, et al. Field test of a reinforced concrete bridge under marine environmental corrosion [J]. Engineering Failure Analysis, 2020, 115: 104669.

[2] Zhang P, Qi Y H, Zou X X, et al. Flexural performance of prefabricated FRP-concrete hybrid beam with in-situ-cast UHPC pockets [J]. Thin-Walled Structures, 2023, 185: 110616.

[3] Dong Z Q, Han T H, Zhang B, et al. A review of the research and application progress of new types of concrete-filled FRP tubular members [J]. Construction and Building Materials, 2021, 312: 125353.

[4] Zou X X, Lin H W, Feng P, et al. A review on FRP-concrete hybrid sections for bridge applications [J]. Composite Structures, 2021, 262: 113336.

[5] Toutanji H, Han M, Gilbert J, et al. Behavior of large-scale rectangular columns confined with FRP composites. Journal of Composite for Construction. 2010,14(1): 62-71.

[6] Yu T, Zhang B, Teng J G. Unified cyclic stress-strain model for normal and high strength concrete confined with FRP [J]. Engineering Structures, 2015, 102: 189-201.

[7] Wang G F, Wei Y, Shen C, et al. Compression performance of FRP-steel composite tube-confined ultrahigh-performance concrete (UHPC) columns [J]. Thin-Walled Structures, 2023, 192: 111152.

[8] Ahmed A, Guo S C, Zhang Z H, et al. A Review on durability of fibre reinforced polymer (FRP) bars reinforced seawater sea sand concrete [J]. Construction and Building Materials, 2020, 256: 119484.

[9] Teng J G, Yu T, Wong Y L, et al. Hybrid FRP-concrete-steel tubular columns: Concept and behavior [J]. Construction and Building Materials, 2007, 21(4): 846-854,

[10] Youm K, Cho J, Lee Y, et al. Seismic performance of modular columns made of concrete filled FRP tubes [J]. Engineering Structures, 2013, 57: 37-50.

[11] Youssf O, Elgawady M A, Mills J E. Displacement and plastic hinge length of FRP-confined circular reinforced concrete columns [J]. Engineering Structures, 2015, 101: 465-476.

[12] Li H J, Chen L C, Ning X Z. A study on seismic behaviour of concrete-filled BFRP tube columns [J]. Journal of Vibration and Shock, 2022, 10: 41. (in Chinese)

[13] Fang S, Liu F, Xiong Z, et al. Seismic performance of recycled aggregate concrete-filled glass fibre-reinforced polymer-steel composite tube columns [J]. Construction and Building Materials, 2019, 225: 997-1010.

[14] Ren F M, Tian S, Ma W, et al. Seismic performance of FRP-confined steel-reinforced RAC columns [J]. Composite Structures, 282, 2022, 115077.

[15] Ren F M, Liang Y, Chen G M, et al. FRP-confined steel-reinforced RAC short columns under eccentric compression: A parametric study and a new design calculation model [J]. Composite Structures, 291, 2022, 115597.

[16] Ren F M, Wu D, Chen G M, et al. Slender FRP-confined steel-reinforced RAC columns under eccentric compression: Buckling behavior and design calculation models [J]. Engineering Structures, 246, 2021, 113059.

[17] Zhang B, Zhou C, Wang C C, et al. Seismic behavior and modeling of elliptical concrete-filled

FRP tubes with longitudinal steel rebars under lateral cyclic load and vertical constant load [J]. Thin-Walled Structures, 2023, 188: 110815.

[18] Zhang B, Peng Y T, Zhang S M, et al. Elliptical concrete-filled FRP tubes with an embedded H-shaped steel under axial compression and cyclic lateral loading: Experimental study and modelling [J]. Composite Structures, 2024, 330: 117839.

[19] Lu X, Mao Y, Chen Y, et al. New structural system for earthquake resilient design [J]. Journal of Earthquake and Tsunami, 2013, 7: 80-616.

[20] Liu X Y, Qin W H, Xu Z D, et al. Investigation on the progressive collapse resistance of three-dimensional concrete frame structures reinforced by steel-FRP composite bar [J]. Journal of Building Engineering, 2022, 59: 105116.

[21] Ahmed A, Guo S C, Zhang Z H, et al. A Review on durability of fibre reinforced polymer (FRP) bars reinforced seawater sea sand concrete [J]. Construction and Building Materials, 2020, 256: 119484.

[22] Ge W, Zhang J, Cao D, et al. Flexural behaviors of hybrid concrete beams reinforced with BFRP bars and steel bars [J]. Construction and Building Materials, 2015, 87: 28-37.

[23] Al-sunna R, Pilakoutas K, Hajirasoulihaet I, et al. Deflection behaviour of FRP reinforced concrete beams and slabs: an experimental investigation [J]. Composite Part B-Engineering, 2012; 43(5): 2125-34.

[24] Dong Z Q, Wu G, Zhao X L, et al. Durability test on the flexural performance of seawater sea-sand concrete beams completely reinforced with FRP bars [J]. Construction and Building Materials, 2018; 192: 671-82.

[25] Ge W, Han M, Guan Z, et al. Tension and bonding behaviour of steel-FRP composite bars subjected to the coupling effects of chloride corrosion and load [J]. Construction and Building Materials, 2021 (296): 123641.

[26] Sun Z, Wu G, Wu Z, et al. Seismic Behavior of Concrete Columns Reinforced by Steel-FRP Composite Bars [J]. Journal of Composites for Construction, 2011, 15(5): 696-706.

[27] Wu G, Sun Z Y, Wu Z S, et al. Mechanical properties of steel-FRP composite bars (SFCBs) and performance of SFCB reinforced concrete structures [J]. Advances in Structural Engineering, 2012, 15(4): 625-636.

[28] Richard P, Cheyrezy M. Composition of reactive powder concretes [J]. Cement and Concrete Research, 1995, 25(7): 1501-1511.

[29] Azmee N M, Shafiq N. Ultra-high performance concrete: From fundamental to applications [J]. Case Studies in Construction Materials, 2018, 9: e00197.

[30] Du J, Meng W N, Khayat K H, et al. New development of ultra-high-performance concrete (UHPC) [J]. Composite Part B-Engineering. 2021, 224: 109220.

[31] Wang Y, Li X, Liao T Y, et al. Axial compressive behavior of high-strength steel-UHPC-clad steel composite walls [J]. Thin-Walled Structures, 2024, 197: 111588.
[32] Azmee N, Shafiq N, Ultra-high performance concrete: From fundamental to applications [J]. Case Studies in Construction Materials, 2018, 9: e00197.
[33] Ebrahim A A, Ge Y, Zhang Z, et al. Flexural Behavior of Reinforced UHPC Beam with SFCBs [J]. Case Studies in Construction Materials, 2022, 16: e01110.
[34] Yan W, Zhang R, Sushant S. et al. Experimental investigation on flexural performance of UHPC beams reinforced with steel-FRP bars [J]. Archives of Civil and Mechanical Engineering, 2024, 24, 132.
[35] JGJ 55-2019, Specification for mix proportion design of ordinary concrete [S]. Beijing: China Architecture and Building Press, 2019. (in Chinese)
[36] GB/T 31387-2015, Reactive powder concrete [S]. Beijing: Standards Press of China, 2015. (in Chinese)
[37] GB/T 50081-2019, Standard for test methods of concrete physical and mechanical properties [S]. Beijing: China Architecture and Building Press, 2019. (in Chinese)
[38] T/CCPA 7-2018/, T/CBMF 37-2018, Fundamental characteristics and test methods of ultra-high performance concrete [S]. Beijing: China Architecture and Building Press, 2018. (in Chinese)
[39] ASTM D7205/D7205M-21, Standard Test Method for Tensile Properties of Fiber Reinforced Polymer Matrix Composite Bars, Annual Book of ASTM Standards [S]. ASTM, West Conshohocken. PA. 2021.
[40] Wu G, Wu Z S, Luo Y B, et al. Mechanical Properties of Steel-FRP Composite Bar under Uniaxial and Cyclic Tensile Loads [J]. Journal of Materials in Civil Engineering, 2010, 22(10):1056-1066.
[41] GB/T5350-2005, Fiber-Reinforced Thermosetting Plastic Composites Pipe: Determination for Longitudinal Compressive Properties [S]. The Standards Press of China, 2005. (in Chinese)
[42] ASTM D2290-19a, Standard Test Method for Apparent Hoop Tensile Strength of Plastic or Reinforced Plastic Pipe by Split Disk Method, American Society for Testing and Materials (ASTM), Philadelphia, USA, 2019.
[43] GB/T 228.1-2021, Metallic materials—Tensile testing—Part 1: Method of test at room temperature [S]. The Standards Press of China, 2005. (in Chinese)
[44] Zhang B, Gao Y H, Peng Y T, et al. Seismic performance of circular concrete-filled FRP tubes consisting of H-steel with shear studs: Experimental study and numerical modelling [J]. Thin-Walled Structures, 2023, 193: 111225.
[45] JGJ 101-2015, Specification for seismic test of buildings [S]. Beijing: China Architecture and Building Press, 2015. (in Chinese)

[46] Zhang Z Y, Guo X Y, Yang Z X, et al. Experimental investigation on the seismic performance of square concrete/ECC filled stiffened high-strength steel tubular columns [J]. Engineering Structures, 314, 2024, 118341.

[47] Park R. State of the art report ductility evaluation from laboratory and analytical testing [C]. Proceedings of Ninth World Conference on Earthquake Engineering, Tokyo, Kyoto, Japan, 1988: 605-616.

[48] Feng P, Cheng S, Yu T. Seismic performance of hybrid columns of concrete-filled square steel tube with FRP-confined concrete core [J]. Journal of Composites for Construction, 2018, 22(4): 04018015.

[49] Lam L, Teng J G. Stress-strain model for FRP-confined concrete under cyclic axial compression [J]. Engineering Structures, 2009, 31(2): 308-321.

[50] Teng J G, Lam L, Lin G, et al. Numerical Simulation of FRP-Jacketed RC Columns Subjected to Cyclic and Seismic Loading [J]. Journal of Composites for Construction, 2016, 20(1): 04015021.

[51] Yassin M H M. Nonlinear analysis of prestressed concrete structures under monotonic and cyclic loads [D]. University of California at Berkeley, California, USA, 1994.

[52] Menegotto M, Pinto P E. Method of analysis for cyclically loaded reinforced concrete plane frames including changes in geometry and non-elastic behavior of elements under combined normal force and bending[C]. Libon, 1973.

[53] Zhao J, Sritharan S. Modeling of strain penetration effects in fiber-based analysis of reinforced concrete structures [J]. ACI Structural Journal, 2007, 104(2): 133-141.